Astrometric Detection of Gravitational Light Deflection by Jupiter with Gaia Data

Adriaan-Alexander Ludl

Lund Observatory
Lund University

2011-EXA58

Degree project of 30 higher education credits (for a degree of Master)
September 2011

Lund Observatory
Box 43
SE-221 00 Lund
Sweden

Astrometric Detection of Gravitational Light Deflection by Jupiter

Adriaan-Alexander Ludl[1,2]

Supervisors: David Hobbs[1] and Lennart Lindegren[1]

[1]Department of Astronomy and Theoretical Physics,
Lund University, Lund, Sweden

[2]Institut Supérieur de l'Aéronautique et de l'Espace,
Formation Supaéro, Toulouse, France

Abstract

Gravitational light deflection in the Solar System can be detected by high precision astrometric measurements. We discuss the parametrized post-Newtonian framework and the comparison of metric theories of gravity. At the precision of a few micro-arcseconds, Gaia data will permit tests of the PPN parameters β and γ and to distinguish monopole and quadrupole gravitational light deflection. Accounting for relativistic effects is necessary to achieve the aimed for precision. The theoretical formulation of light deflection is discussed. We deduce an expression for the source direction derivatives required by the AGIS scheme in a simplified relativistic model. This model accounting for monopole and quadrupole deflection terms has been implemented in AGISLab. We have validated the implementation and maintain convergence of the astrometric solution for Gaia. We investigate the precision of the determination of PPN γ with Gaia data for the Sun and planets using the new relativistic model for source direction computations. Simulations in AGISLab show that previously obtained precision for PPN γ can be matched. Full precision Gaia data should allow for a determination down to 10^{-6}. We performed realistic simulations including observation noise and conclude that quadrupole effect remains detectable with a 6σ confidence level even for a 5 arcsec radius of the exclusion zone around Jupiter.

Contents

« ubi materia, ibi geometria »

Johannes Kepler's Thesis XX from
De fundamentis astrologiae certioribus

1 Introduction

Determining the positions and motions of stars and other stellar objects with ever greater precision has been a task of paramount importance in astronomy over thousands of years and has spawned manifold discoveries. The study of kinematic and dynamic properties of stars has allowed a deeper understanding of their physical properties such as their spectra and their sizes. The Gaia satellite mission provide be an astrometric survey of one billion stars at a precision of a few micro-arcseconds. We here discuss the influence of gravitational light deflection on the data reduction for Gaia and how this can be used as a test of general relativity and competing theories.

Measurement of gravitational light deflection by the Sun and the planets of the solar system constitutes a test of general relativity and its extensions. All light deflection measurements to date only allow to confirm the correctness of the monopole light deflection predicted by general relativity. The quadrupole light deflection however has not yet been measured. It serves as a test of General Relativity and other contending theories of gravitation.

1.1 Scope of this work

The objective of this six months project is to simulate gravitational light deflection by the Sun and the planets of the solar system and to study the detection of these effects by the Gaia mission. The goal is to determine the possibility to constrain post Newtonian models of gravity.

In section 2 we present the astrometric problem in the context of the Gaia mission. We describe its main features which will make it possible to achieve the aimed for precision.

We will discuss the equations of gravitational light deflection in section 3. The theoretical foundations and experimental evidence leading to general relativity and competing theories of gravity are examined. Then the parametrized post Newtonian framework described in Will [1993] is introduced. It allows for the predictions of general relativity and other metric theories to be compared.

In section 4 we will describe the implementation of relativistic model in AGISLab and discuss the effects of monopole gravitational light deflection in the data reduction for Gaia. We will present our results on the determination of PPN γ and the detection of quadrupole light deflection.

The appendices give acronyms and notations, units and quote the full parametrized post-Newtonian framework as described by Will [2006].

2 Astrometry

2.1 Historical overview of astrometry

What is astrometry? Astrometry is the discipline concerned with the study and measurement of the kinematic and dynamic properties, and the brightness (magnitude) of celestial bodies. Among those properties are the positions and motions of objects, as well as their size [Kovalevsky, 2002]. The development of astronomy and astrometry is tightly linked to the compilation of star catalogues. They can be traced back to Timocharis, Aristillus and Hipparchus in the second century BC, and have gradually increased in size. Their form has changed from hand written recordings on papyrus or paper to globally accessible digital databases such as Simbad. Today these are updated daily and incorporate data from satellite missions such as HIPPARCOS.

A catalog provides the identification of stars and their positions. This allows one to track the motion of stars and the evolution of their physical characteristics. [Perryman, 2010]

The increase in precision of measurements has spawned discoveries of new phenomena and objects, such as the precession of orbits, the structure of the galaxy, the motion of the Sun around the center of the Milky Way galaxy, and the discovery of other galaxies.

The kinematic properties are the positions and motions of the planets. The sky is usually mapped by a spherical coordinate system consisting of two angles describing an object's orientation on the sky and the third coordinate being the distance to the origin. The proper motion of an object is the variation of these three parameters. A more detailed discussion of coordinate systems and reference frames can be found below.

The dynamic properties are found from the variations in the time series of observations. They are described by their apparent acceleration. The precise determination of all of these needs careful transformation between different reference frames to take into account relativistic effects.

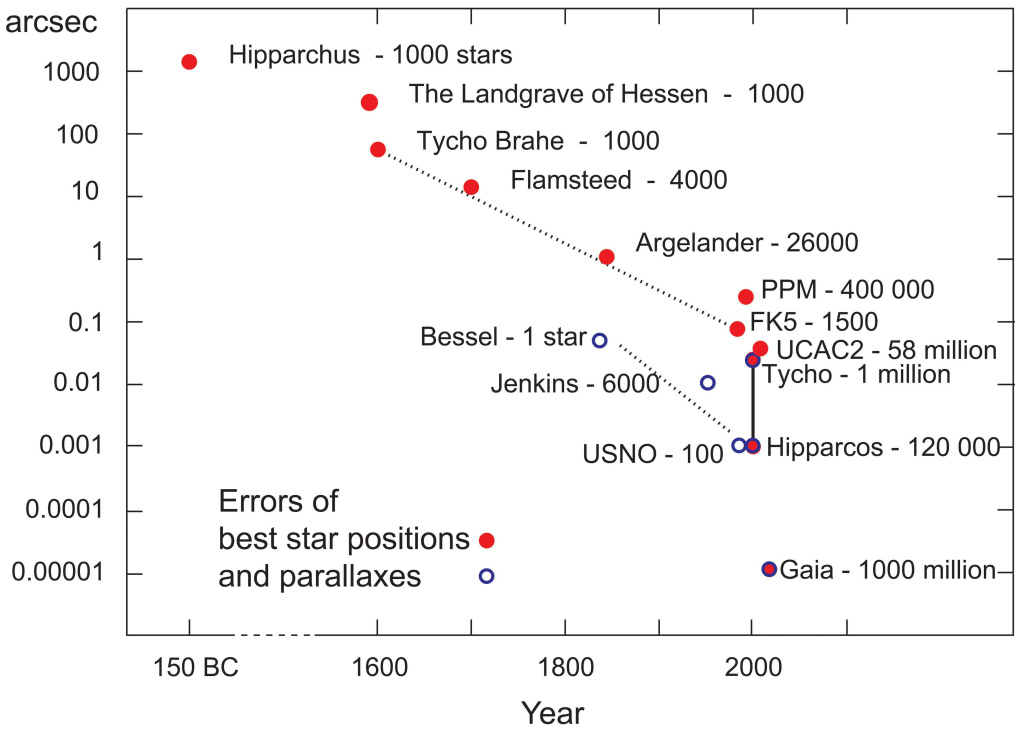

Figure 1: Diagram illustrating the progress in astrometric accuracy from Hipparchus to Gaia. The latter space astrometry mission will push astrometric measurements to the limits. (Jos de Bruijne, 2009, ESA Science Team [2010] [2])

Objects studied in astrometry Star maps and catalogs describe the positions and motions of celestial objects. To give but a brief overview of the different kinds of objects, a more detailed one can be found in most modern astronomy textbooks (for instance [Kovalevsky, 2002]).

- planets : "wandering" objects which move quickly compared to an apparently fixed background
- stars : on short time scales these appear to be fixed on the celestial sphere and are small and possibly bright objects. They are self gravitating balls of gas.
- diffuse objects such as nebulae, clusters, galaxies which may be composed of hot gas, dust, or large numbers of stars

The Milky Way has three structural components: the flat disc, the bulge and the halo. The flat disc contains nearly 10^{11} stars of all spectral types and ages orbiting the Galactic centre. The bulge is less flattened, supposedly contains a supermassive black hole and may contain a bar. The halo surrounds the disc and bulge, has roughly 10^9 stars, which are old and metal poor, as well as approximately 160 globular clusters and a small number of satellite dwarf galaxies. This entire system is embedded in a massive halo of dark material of unknown composition and poorly known spatial distribution [Jos de Bruijne, GAIA: Galactic Structure in Gaia Infosheet 2009][2]. The internal physical properties of these objects are not the subject of study of astrometry and will not be further discussed here.

The main concern of astrometry is the precise measurement of positions and motions of these objects. These are expressed in a reference frame. The sky is mapped by a spherical coordinate system consisting of two angles describing an object's orientation on the sky and the third coordinate being the distance to the origin. This is discussed in in further detail in section 3.2.4 of Ludl [2011].

Astrometry and relativity In the history of scientific thought considerable effort has gone into devising a simple elegant description and model of planetary motion. The Keplerian revolution and Newton's law of gravitation provided a unified framework for astrometric calculations and provided a basis for new discoveries. The ideas at the heart of special and general relativity originate in the same search for a simple geometrical description of reality on all scales. These theoretical frameworks have allowed to explain phenomena which had hitherto remained mysterious such as the perihelion precession of Mercury. The latter is a small effect ($43''$ per century) and highly accurate instruments and techniques are required to obtain precise measurement.

The main principle of relativistic theories is the principle of equivalence, which contains the assumption of constant speed of light. This is further discussed in section 3.2.1 of Ludl [2011].

The ties between astrometry and relativity lie in the experiments. Today's precise astrometric measurements require models which take into account relativistic effects. This in turn allows to test the predictions of special and general relativity. The Eddington experiment performed during the 1919 solar eclipse measured the light bending by the Sun. It was one of the first tests of the general theory of relativity, although the quality of the data has been the subject of dispute. Today the improvements in experimental techniques have allowed to place constraints on the validity of general relativity and to test its predictions against those of alternative theories. The upcoming Gaia mission will survey the sky and permit tests of general relativity to higher precision. One of these is the measurement of gravitational light deflection by Jupiter which is the subject of this project.

[2] `http://www.rssd.esa.int/index.php?project=GAIA&page=Info_sheets_overview`

Hipparcos and subsequent catalogs Earth bound astrometry was limited by effects such as atmospheric variability and seismic perturbations. The motivation behind the Hipparcos mission was to lift these limits by making high precision astrometry space-borne to avoid these limitations.

Hipparcos (High Precision Parallax Collecting Satellite) was a satellite mission of the European Space Agency during the 1990's. It produced a three-dimensional map of the sky. The first catalog produced using this data, the Hipparcos catalog contains 117 955 stars with astrometric data. The positions are accurate to better than 2 milli arcseconds, which is about a factor 100 better than can be obtained from Earth based observatories. The project also produced the Tycho catalog. It is more complete since it contains more than two million additional stars, but their astrometric data is less precise. [Perryman, 2010]

2.2 Gaia and current missions

2.2.1 The Gaia mission

The ESA mission Gaia has been designed with a view to survey our galaxy, the Milky Way. It will yield a star catalog with a precision of 8–25 μarcsec(μas) and will encompass stars down to magnitude 20 [Prusti, 2011]. Originally GAIA was an acronym for: Global Astrometric Interferometer for Astrophysics. As the mission has increased in complexity and different choices in technological implementation have been made, this has become obsolete. The idea of the mission was originally outlined in Lindegren et al. [1992] as a successor to ESA's Hipparcos mission. The mission was approved by ESA in 2000. The launch is planned for 2013 and the five years of observations are to start by 2014. The nominal duration of the mission is five years.

The scientific objectives of the Gaia mission are far reaching. The study of the Milky Way galaxy and its origin lie at their heart. Aside from the study of galaxy formation and galactic dynamics, it will provide statistics on many stars and thereby help to improve the understanding of stellar physics and evolution. The objects to be detected are also expected to be of all classes of astrophysical objects including brown dwarfs, white dwarfs, and planetary systems. The Gaia mission will also allow us to carry out a new Solar System census. Moreover the results of Gaia will contribute to the understanding of fundamental physics. In particular, high precision astrometry, that is precise angular distance and motion measurements will allow us to test General Relativity against competing theories of gravitation, which can be expressed in the parametrized post-Newtonian formalism (PPN gamma). This is discussed in more detail in Ludl [2011] section 3.2.3.

It will deliver a catalogue of about one billion stars in the Milky Way galaxy down to magnitude 20. The expected precision will allow to improve the distance scale of the Galaxy and the universe. It is expected that this will result in a three dimensional structural map of one billion stars in our galaxy, an improvement on the Hipparcos catalog by a factor of about ten thousand.

2.2.2 The Gaia satellite

Mechanics and orbit: The main structural element of Gaia is the silicon carbide torus, on which the instruments are mounted. The satellite will be in orbit around the Lagrange point L_2 of the Sun-Earth system. Its orbit is designed to allow it to scan the whole sky such that every object will be observed about 70 times.

- spinning on its axis at 6h for a full circle
- spin axis precessing a full circle in 63 days
- the orbital motion around the Sun in one year

These three motions allow an almost homogeneous coverage of the sky. On average 70 observations per source over the five year mission will be obtained.

At the second Lagrange point (L_2) Gaia will be in a nearly periodic Lissajous orbit, which is stable and avoids the need for large maneuvres. Small maneuvres will be required roughly one a month. This orbit also helps to avoid the eclipse zone during the mission. This is essential for the solar panels that generate power, and to keep the thermal environment stable. The selection of the orbit arose from a trade-off between communication, operations, cost, thermal and radiation environment, and accessibility with current rockets.

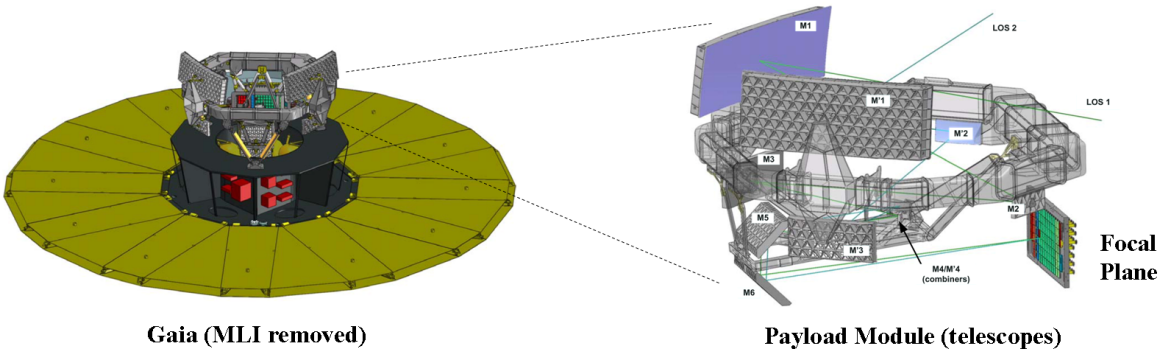

Figure 2: At the left, overview of the Gaia satellite showing the space craft and payload on top. A zoom on the payload module at the right shows the two main mirrors $M1$ and $M1'$ and focal plane (Copyright ESA).

Optics and detectors: There are three instruments in the payload on board Gaia. They will carry out astrometry, photometry and spectroscopy.

Here we shall give a brief overview of the science that the photometry and spectroscopy instruments will do and the general error requirements. Gaia will observe in the visual spectrum, in the magnitude range from 6 to 20. For astrometry the precision of the data will depend on the magnitude of the star. The parallax error is to be around 7 μarcsec for the brightest stars ($G < 13$)[3], 20μas (microarcseconds) at 15 mag, and 200μas at 20 mag. The photometric instrument will allow the determination of stellar surface parameters. It is designed to give temperatures to a few hundred Kelvin, gravities and metallicities to 0.2 dex. Thus the requirements on its sensitivity are: 8 to 20 mmag for a 15 mag star. The spectroscopic instrument is necessary for the determination of radial velocities of objects. It is designed for a precision better than 1 km/s for bright stars (V<13.5 mag), covering wavelengths from 330 to 1000 nm. The signal to noise ratio (S/N) of the spectroscopic instrument is required to be at resolution

[3]Here we use G to denote Gaia magnitudes. The definition of G and the transformation to other magnitude scales, is beyond the scope of this work. They are discussed briefly in Bastian [2007], and more extensively in Jordi et al. [2010].

better than $\Delta\lambda/\lambda = 10\,000$ for deduction of astrophysical parameters for a subsample of the sources [Prusti, 2011].

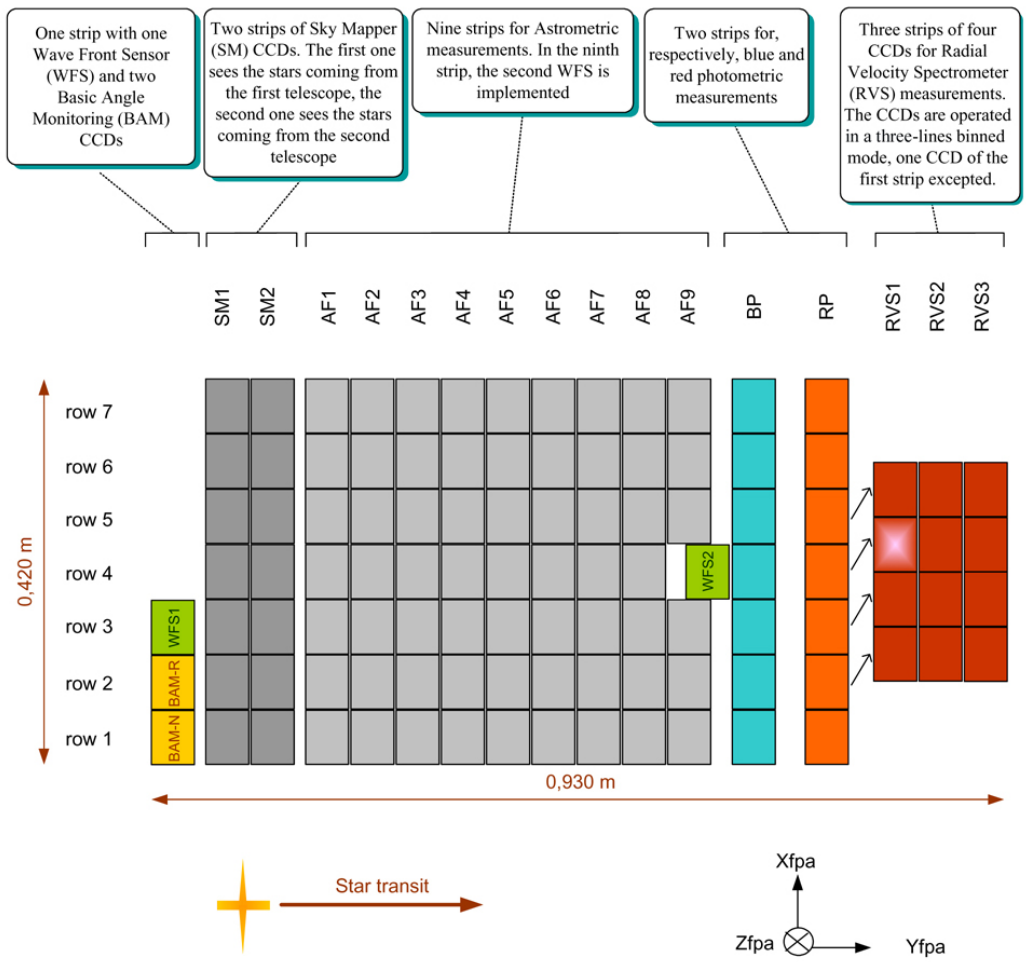

Figure 3: This diagram shows the CCD layout in focal plane of Gaia, with the astrometric field in light gray at the center. (Copyright EADS Astrium)

2.2.3 Limitations of the Gaia mission

There are technical limitations to the data Gaia will deliver. One of these is related to the filters used, they determine the observable wavelengths.

According to [Prusti, 2011] the problems are mainly of the following types. It is difficult to meet the astrometric precision requirements for blue stars, the reference star is B1V and the deviation is about 10% for the parallax error. Another class of stars that have high errors are those of magnitude $G < 7$ mag, the parallax requirement is missed by 1 to 2μarcsec. This is determined by the gating scheme used in the mission. Another problem is saturation of the CCDs by bright objects, Jupiter has V magnitude in the range of $[-3, -1.6]$ and its angular size is about 40 arcsec. This will result in a temporary blinding of the CCDs and make observations impossible within 5 arcsec of Jupiter. This is an important factor in the measurement of light deflection, mostly for the quadrupole (and weaker) terms [Hobbs et al., 2010, Martin Fleitas et al., 2011]. Additionally there are optical limitations such as the size of the mirrors and CCDs.

How far away can Gaia see into the Milky Way? This depends not only on the technical characteristics, but also on the extinction coefficients of interstellar matter and the direction

in which it is pointed. Distant objects can be seen if they are very bright or magnified by a gravitational lens for instance. What can be ascertained more clearly is the expected fraction of stars/objects/sources in the Milky Way that will be covered by the telescope. Approximately a billion objects in the magnitude range between 6 and 20, this corresponds only to 1% of all objects in the galaxy.

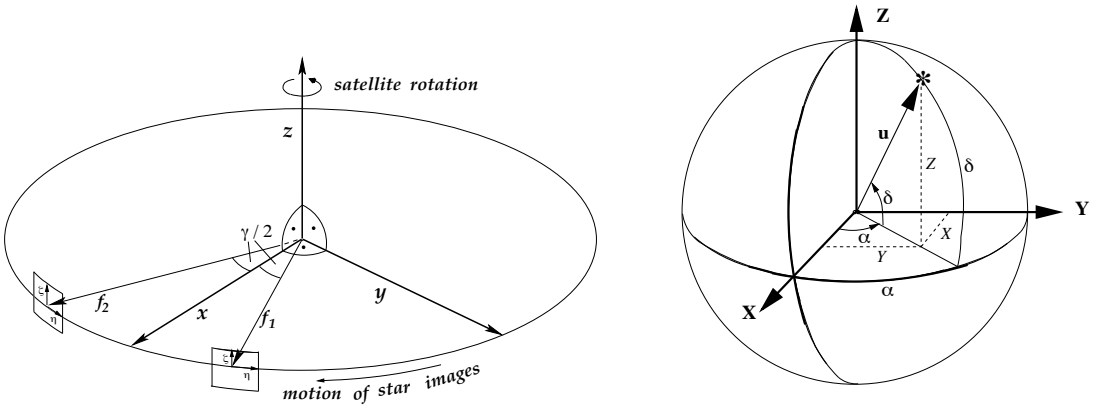

(a) The Scanning Reference System (SRS), the Gaia viewing directions and the Field-of-View Reference Systems (FoVRS). The angles between the two viewing directions are not drawn to scale. The black dots near the centre denote 90°angles (marked by the arcs). The big ellipse indicates the instantaneous scan great circle on the celestial sphere. The small rectangles indicate the fields on the sky; the small arrows show the orientation of the field angles. The principal axes f_1, f_2 of the FoVRS point towards the centre of each field of view. The w and z axes (not labeled in the diagram) point parallel to the η and ζ axes, respectively. The direction to the sun is always at an angle of 45°from the positive z axis.

(b) Illustrative sketch of the celestial sphere indicating the ICRS spherical coordinates (α, δ) and direction cosines (X, Y, Z) of a unit vector u towards a star (upper right), with the origin of (α, δ) at front left and the ICRS north pole towards the top.

Figure 4: The satellite and ICRS frames, both from Bastian [2007]

2.2.4 Scanning space astrometry

Scanning space astrometry is the term designating the kind of astrometric observation used in the Hipparcos and Gaia missions. It relies on the transformation between (linear) positional data and the spinning telescope. We will give an overview here, a detailed account can be found in Lindegren and Bastian [2011] and references therein.

Indeed, as Gaia will be scanning the sky, the precise time when the centre of a star image has some well-defined position in the field of view (FoV) is determined. The position is defined by the pixel layout of the CCDs in Gaia. Then the observation time is the one-dimensional (along-scan, AL) measurement of the stellar position relative to the instrument axes. At the same time an approximate across-scan (AC) position of the star is also measured. However, the AC measurement is less accurate due to the geometry of the CCDs which are elongated in the AC direction, the lower optical resolution across-scan, and the way the pixels are read out. The astrometric catalogue is produced after processing a very large number of such observation times. This process involves a precise reconstruction of the instrument pointing (attitude) as a function of time and of the optical mapping of the CCDs through the telescope onto the celestial sphere.

A number of factors impact the AL measurement. We will discuss the basic angle, the scanning law and parallax determination in the following.

Gaia's two fields of view (FoV) coincide on the focal plane shown in figure 3. The basic angle between them is Γ =106.5°. This choice is motivated by two reasons. The first is to make it as large as possible, the second to avoid divisors of 360°. The accuracy of the one-dimensional AL position measurement depends on the basic angle. In the 1D case there are peaks in the variance of star positions for basic angle values of the kind $\Gamma = m/n$ (rad) with m, n being small integers. These peaks should be avoided. In the case of Gaia we have $m = 71$ and $n = 240$, which are large enough to avoid such problems. It can be noted that this effect disappears for two dimensional measurements when the global solution over the whole celestial sphere is considered. Basic angle variations are unavoidable and have to be monitored, to compensate for the errors they could induce. This should be precise to within 10μarcsec, and will be monitored and measured down to 1μarcsec.

The scanning law describes the attitude of the satellite as a function of time. It gives the transformation between the Gaia proper frame and the reference frame for the catalog (e.g. BCRS). It prescribes the precession rate, the direction of the spin axis $\mathbf{z}$ as a function of time, the spin rate, which for Gaia is $60''s^{-1}$, the phase of the spin at some initial epoch, and solar aspect angle $\xi = 45°$.

To optimize the parallax measurement, large ξ are preferred, however protecting the satellite optics from direct and indirect sunlight imposes the constraint $\xi \leq 45°$. The chosen fixed value is also a factor that contributes to the constant thermal environment.

The spin period of Gaia is $P = 6$hr, the AC size of the FoV is $\Phi = 0.69°$. Preferably the areas of the sky scanned in successive spins should overlap, to avoid the occurrence of gaps. Therefore $|\mathbf{z}| \leq \Phi$ should be verified. This condition is not quite satisfied for Gaia, so there will be gaps. The precession rate is the inverse of the number of loops per year $K = 5.8$ for Gaia.

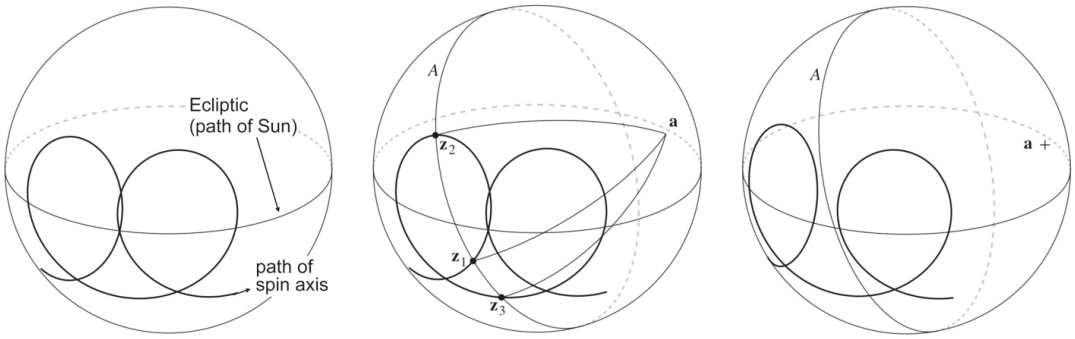

Figure 5: The precession of Gaia's spin axis, from [Lindegren and Bastian, 2011]. The spin axis $\mathbf{z}$ makes loops around the Sun, which must overlap as in the left and middle diagram in order to provide good observing conditions. The star at point $\mathbf{a}$ may be scanned whenever $\mathbf{z}$ is 90° from $\mathbf{a}$, that is on the great circle A at $\mathbf{z_1}, \mathbf{z_2}, \mathbf{z_3}$ and so on.

The resulting "uniform revolving scanning law" is the baseline for both Hipparcos and Gaia, with slightly different parameters.

Lindegren and Bastian [2011] have pointed out that absolute parallaxes are obtained, even though scanning space astrometry also makes purely differential measurements. The principle of the parallax measurement is illustrated in figure 6. In Lindegren and Bastian [2011] this is explained as follows. This is made possible by the measurement of the relative parallax shifts between stars at large angular separations. For an observer at 1 AU from the Sun, the apparent shift of a star due to its parallax ϖ equals $\varpi \sin\theta$ and is directed on a great circle from the star towards the Sun. As shown in figure 6 (left), the AL parallax shift of the star at F is $\varpi_F \sin\theta \sin\psi = \varpi_F \sin\xi \sin\Gamma$, where $\xi = 45°$ is the constant solar aspect angle (between the Sun and the spin axis). At the same time the AL parallax shift of the star at P is zero.

The AL measurement of F relative to P therefore depends on ϖ_F but not on ϖ_P, while the reverse is true at a different time, as shown in the right diagram.

The sensitivity to parallax is proportional to $\sin\xi \sin\Gamma$, which should therefore be maximized. The choice of ξ was discussed above. While $\Gamma = 90°$ is optimal for the basic angle according to this analysis, we have seen that other considerations led to a slightly larger value being adopted for Gaia.

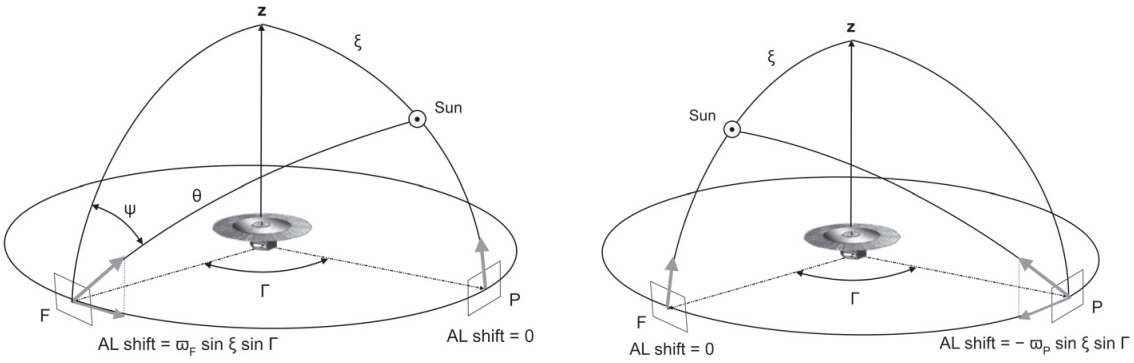

Figure 6: The geometry of the parallax measurement: The measured along-scan (AL) angle between the stars at P, F depends on their parallaxes ϖ_P, ϖ_F in different ways depending on the position of the Sun. This allows to determine their absolute parallaxes rather than just the relative parallax $\varpi_P - \varpi_F$. [Lindegren and Bastian, 2011].

This is relevant to the study of light deflection because the monopole deflection of the Sun is similar to a global shift of the parallaxes [Hobbs et al., 2010].

The parallax shift of a star is directed toward the Sun, as shown by the arrows on F and P in figure 6. The monopole light deflection is a shift of the apparent position of the star away from the Sun (along the great circle). In figure 6 the angle between the Sun and the star F along the great circle is θ. This effect has been shown to result in a statistical correlation of PPN γ and the parallax zero point [Mignard, 2002]. Both shifts have to be taken into account to determine the correct direction toward the star. These two shifts differ in their dependence on the angular separation from the Sun, this property is used in the data processing chain to distinguish them and determine the value of PPN γ for the Sun.

2.3 Data processing : AGIS, AGISLab and GREM

Gaia will produce a large amount of data, approximately 40Gb of telemetry data per day and an estimated 100 Tb over the 5 year mission. (Uwe Lammers, *Gaia: Astrometric Data Reduction* ESA Science Team [2010]) To cope with the data processing the Gaia Data Processing and Analysis Consortium (DPAC) has been formed in 2006 to structure the Gaia working groups and the efforts of the scientific community across Europe (M. Perryman, 2006, ESA Science Team [2010]). DPAC is in charge of the data reduction for Gaia. This comprises astrometric data reduction and the reduction of spectroscopic and photometric data. Among these are binary recognition, search for moving objects and exoplanets.

The main steps of the data processing chain are shown in figure 7. There are two phases the daily data processing and the Astrometric Global Iterative Solution (AGIS). The Initial Data Treatment (IDT) first processes the daily telemetry data, which evaluates the astrometric image parameters using the raw CCD data. The output of IDT is fed to the One Day Astrometric Solution (ODAS) which is part of Gaia's First-Look (FL) system. It evaluates the source parameters, the satellite's attitude and calibration parameters to sub-milli-arcsec accuracy. The daily results are then written into the Main Data Base (MDB). (Uwe Lammers, *Gaia: Astrometric Data Reduction* ESA Science Team [2010])

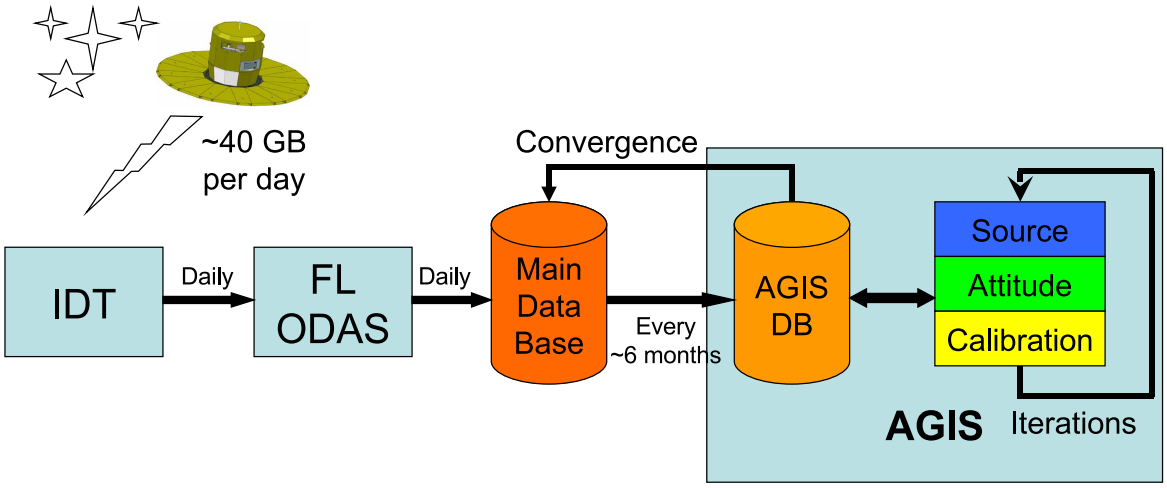

Figure 7: This diagram shows a schematic overview of the astrometric data processing chain for Gaia. The main units are IDT, FL-ODAS and AGIS which are described above. IDT and FL-ODAS perform preliminary evaluation of data and astrometric parameters. AGIS will generate the final astrometric mission products every six months and on the final data set. (Credit: Uwe Lammers ESA Science Team [2010])

2.3.1 AGIS and AGISLab

The MDB will accumulate data constantly, it is this data which is the input to AGIS, the core data processing module, which will analyse this data every 6 months. It produces a "Gaia catalog" with expected accuracies of 8–25 μarcsec (μas) for trigonometric parallaxes, positions at mean epoch and annual proper motions of simple stars[4] [Lindegren et al., 2011, p. 1] The subset of well-behaved primary stars is now believed to be substantially larger than 100 million [Lammers and Lindegren, 2011].

The determination of the "core solution" is an exceedingly difficult task, since there are very large quantities of data involved and due the complexity of the relationships between astrometric, spectroscopic and photometric data, as well as data collected at different epochs.

[4] i.e. apparently single stars

The astrometric core solution determines the five astrometric parameters for the primary stars. The direct resolution of the overdetermined problem involving about 10^{12} measurements and roughly $5 \cdot 10^9$ unknowns is unfeasible, despite the sparse nature of the matrix (figure 8). AGIS minimises the merit function χ in a least squares algorithm.

$$\chi^2(X) = \sum_i \frac{R_i(X)^2}{\sigma_i^2 + \epsilon_i^2} w \left(\frac{R_i(X)}{\sqrt{\sigma_i^2 + \epsilon_i^2}} \right) \tag{1}$$

where X is the vector containing the unknowns, i is the observation index, R_i the residuals, σ_i the formal observation certainty, ϵ_i the excess noise, and w the down-weighting function. This formula is discussed in Lammers and Lindegren [2011].

From equation (1) the standard system of normal equations for source, attitude and calibration parameters is deduced. This system can be solved by iterating in a straight forward way. In practice alternating phases of "Simple Iterations", "Accelerated Simple Iterations" and Conjugate Gradient iterations have been employed. There is a large number of unknowns, approximately: $5 \cdot 10^8$ source parameters, $4 \cdot 10^7$ attitude parameters and 10^6 calibration parameters. To this a small set of global parameters may be added [Lammers and Lindegren, 2011]. (PPN γ is discussed in section 3.2.3 of Ludl [2011].) A global normal matrix can also be deduced when the global parameters are solved for, the global normal equation is given as equation (90) in Lindegren et al. [2011]. At least as many measurements as unknowns are needed to obtain an accurate solution. Consequently, AGIS will be executed only about once every 6 months, when enough data has been collected. This choice was made, considering the number of operations needed for the solution (expected to be some 10^{20} FLOPS) and the expected increase in precision achievable. One full run at the end of the mission is estimated to take about 2 months on a 10 TFLOP/s processing system. Further discussion of the complexity of the astrometric problem can be found in Bombrun et al. [2010].

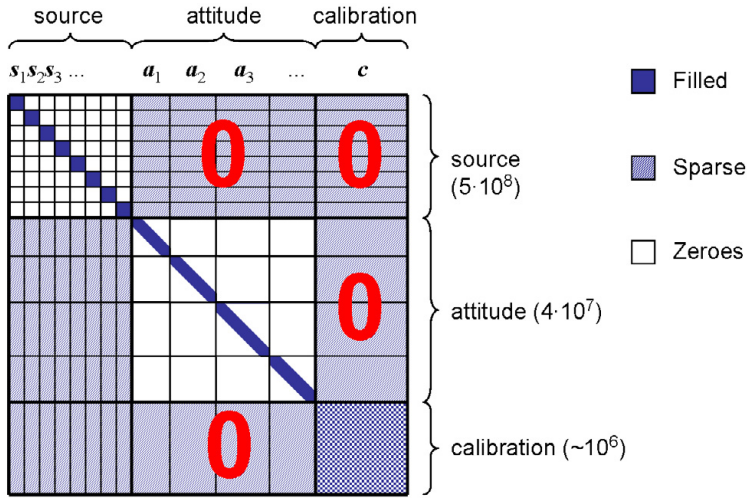

Figure 8: The structure of the normal equation matrix to be solved with AGIS. Setting four of the off-diagonal block to zero (red figures) gives the Gauss-Seidel pre-conditioner. Numbers in braces indicate the number of parameters of each kind. Lammers and Lindegren [2011]

AGISLab is a scaled version of AGIS developement mainly by Holl, Hobbs and Lindegren in Lund. It can run on less than 10^6 stars and therefore allows a significant number of Monte Carlo simulations with different noise realisations to be made in a relatively short time [Holl et al., 2010].

The scaling parameter is S, the simulations run in AGISLab use a fraction S of the total number of sources. AGISLab is designed to modify the Gaia layout in such a fashion that

certain quantities of interest for data analysis are conserved. This is achieved by reducing the focal length of the telescope and its spin rate, whereby "the mean number of stars in the focal plane at any time, the mean number of field transits of a given star over the mission, and the mean number of observations per degree of freedom of the attitude model " are conserved [Holl et al., 2010].

Building on the work in Hobbs et al. [2010], we have studied the possibilities of measuring light-deflection and PPN γ with Gaia by expanding the model for gravitational light deflection used in AGISLab.

2.3.2 Gaia relativity models

The resolution of the astrometric problem for Gaia, requires a consistent treatment of source parameters in a relativistic framework. As described in Crosta and Vecchiato [2010], there are currently two models that permit to obtain this solution with microarcsecond precision: GREM and RAMOD.

The baseline relativity model for Gaia is the Gaia Relativistic Model (GREM). This framework is built on the post-Newtonian approximation of metric theories of gravity[5] and the parametrized post-Newtonian formalism. It takes into account light deflection and other relativistic effects inside and outside the Solar System. These effects are treated as perturbations to the assumed solution (source direction) outside the Solar System [Crosta and Vecchiato, 2010, Klioner, 2003, 2008]. This is akin to the model we solve in the PPN formalism (see section 3.2.5).

The Relativistic Astrometric Model (RAMOD) follows a different approach. It solves the inverse ray tracing problem for general relativity. It is not constrained to approximations and this allows to probe the predictions of general relativity specifically. [Crosta and Vecchiato, 2010]

The advantage of GREM is that it allows to directly compare the different viable theories of gravitation and to place boundaries of the PPN parameters [6]. Both models are designed to be used for Gaia data reduction, thus is it essential that their results can be compared. Crosta and Vecchiato [2010] discuss a comparison between the two frameworks.

In the next section we will present a model of light deflection based on [Crosta and Mignard, 2006] and accounting for monopole and quadrupole light deflection. This model will be implemented into AGISLab to perform realistic numerical simulations of the astrometric solution on Gaia data. The quadrupole effect is also studied by the Gaia Relativistic Experiment on Quadrupole light deflection (GAREQ formerly GAREX). We believe that the comparison of our results to the preliminary results of these more complete models will prove to be beneficial.

[5] See section 3.2.1 of Ludl [2011] for a definition of metric theories of gravity of which general relativity is one example.

[6] The parametrized post-Newtonian framework and parameters (PPN) are discussed in section 3.2.3 of Ludl [2011].

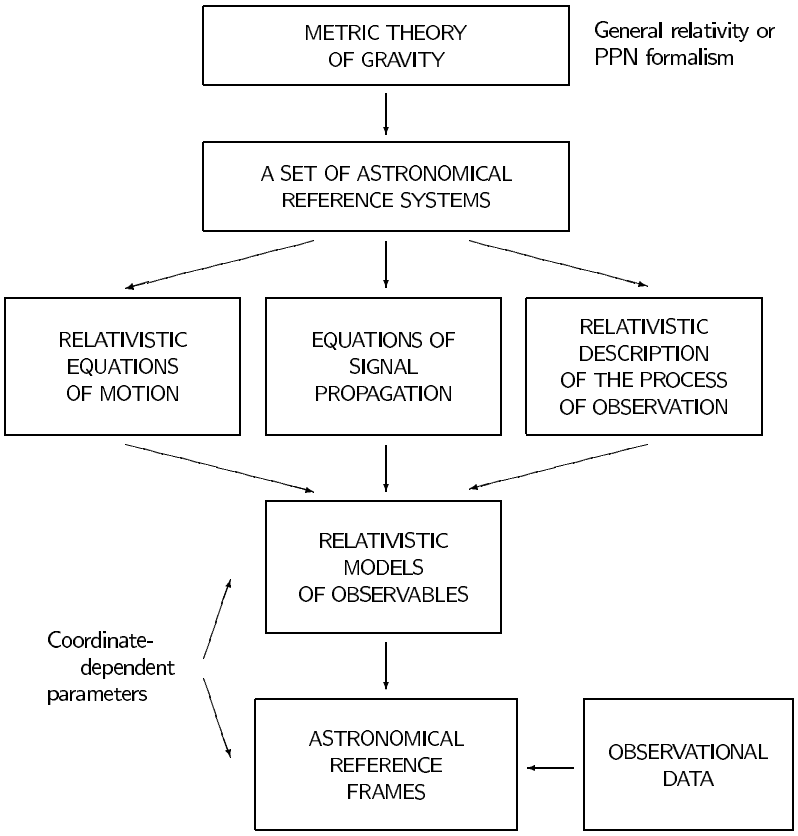

Figure 9: Representation of the general principles underlying the relativistic modeling of astronomical observations. Klioner [2003]

3 Gravitational light deflection

3.1 Light bending and experimental tests of relativity

This foundations of relativistic models and metric theories of gravity are discussed in greater detail in the first report. Here we present the classical tests of light deflection and the equation implemented in AGISLab.

3.1.1 Experimental tests of general relativity

We will present the three classical tests of general relativity and then discuss more recent ones. In the solar system, the predictions of general relativity are in good agreement with Newtonian mechanics and observations. Most planetary orbits are in good agreement with both theories. However there are three instances of physical effects which have helped establish general relativity as a more correct theory than its predecessor. They are: Mercury's perihelion precession, the light deflection by the Sun for grazing rays and gravitational redshift of light. All of them are relatively small effects.

According to Kepler's second law, planet's move on elliptical orbits around the Sun. In Newtonian mechanics, these orbits are perturbed by the small gravitational pull of the other planets. According to Will [1993, p. 4] the three strongest contributions to the rate of precession of Mercury, as predicted by Newtonian theory are due to Venus, the Earth and Jupiter. After summing the contributions of all planets a discrepancy of $42.7''$ per century remains. The presence of this advance was first noted by Le Verrier in 1859. The value is close to the prediction from general relativity which is $42.95''$ per century.

This effect can be explained heuristically by two contributions. The first is the special relativistic mass increase of the planet. The second is due to the mass associated with the energy density of the Sun's gravitational field. This term adds to the Sun's gravitational potential in the Newtonian picture. This is discussed in further detail in Sexl and Sexl [1979]. Will notes that the solar quadrupole moment may also contribute to this shift. From helioseismic measurements and assumptions about the internal structure of the Sun it has been inferred that its quadrupole moment is $J_2 = (2.2 \pm 0.1)\,10^{-7}$ [Roxburgh, 2001]. The correction to the precession rate is smaller than experimental errors, hence general relativity passes this test.

The second classical test is the deflection of light by massive objects. Interest in this weak phenomenon was restored by the advent of general relativity. In the solar system the most massive body is the Sun, therefore the deflection due to the Sun was studied first. Notably the 1919 solar eclipse and Eddington's expedition caught public attention. The experiment was performed by two teams in Sobral in Brazil and on the Island of Principe off the Atlantic coast of Africa and measured the displacement of stars close to the Sun. Due to the limitations in optical equipment at the time, observations had to be made during a total eclipse when the Moon blocks out direct Sun light and the field of stars in its vicinity becomes visible. The observations were recorded on photographic plates and compared to records of the same field when the Sun was not present. The results were given as 1.13 ± 0.07 and 0.92 ± 0.17 times the value predicted by Einstein (1.75 arcseconds) [Will, 1993, p. 5]. This value is twice that obtained by Soldner using the Newtonian theory. These results were questioned and indeed offered only weak agreement compared with modern ones. During the 1970's they were finally confirmed with a precision of 1% using radio wave interferometry. A pair of experiments was carried out using a radio interferometer of 35-km base-line at the National Radio Astronomy Observatory (NRAO) in 1974 and 1975. The set up differed also in the angles between the sources and the Sun, nonetheless according to [Fomalont and Sramek, 1976], "the mean gravitational deflection is 1.007 ± 0.009 (standard error) times the value predicted by general relativity". It also gave an estimate of the post-Newtonian parameter $\gamma = 1.014 \pm 0.018$ (standard error) and the corresponding absolute value of deflection at the

solar limbs of 1.761 ± 0.016 arcseconds.

This effect has also been employed in the data reduction for Hipparcos and will be for Gaia. The equations describing the phenomenon will be developed later in the parametrized post-Newtonian formalism in section 3.2.5.

The third classical test is gravitational red shift of light. This was the first to be proposed by Einstein himself. Since it is a test of the equivalence principle, we shall discuss it in sections 3.2.1 and 3.2.2 of Ludl [2011].

Will proposed the time delay of light as a third classical test of general relativity, instead of the red shift experiment for which the predictions of every metric theory of gravitation are identical. In 1964 Irwin Shapiro discovered that a ray of light propagating in the gravitational field of a massive body will traverse a given distance in a longer time, than if the field were absent. In the decades following the discovery of this effect a number of solar system experiments have been carried out. What is measured is the round trip time of a signal emitted from Earth and reflected from another body (planet or space craft). Radar ranging of targets was commonly used. A detailed discussion can be found in Will [1993, p. 173]. It is one of the most precise tests of general relativity. Time delay has also been exploited in the Cassini 2002 Solar Conjunction Experiment which gave the limit $\gamma - 1 \leq 2.3 \cdot 10^{-5}$. This experiment if discussed in more detail in section 3.2.3 of Ludl [2011].

During the second half of the 20^{th} century, gravitational lensing and gravitational waves emerged as fields of application of general relativity. Both are linked to extragalactic astrophysics.

The idea that the gravitational bending of light is similar to the action of optical lenses goes back to the earlier years of the theory. It was realised that multiple images of an object can be formed. In 1937 Zwicky predicted gravitational lensing by galaxies and expected the phenomenon to be observable. However the phenomenon was not observed until 1979, when Walsh, Carswell and Weyman detected the first gravitational lens candidate with multiple images. In 1987 Lynds and Petrosian announced "luminous arcs": highly distorted images of high redshift galaxies. Ringlike deformed objects were finally discovered in 1988. An account of the historical evolution of ideas can be found in the introduction of Schneider et al. [1992].

Gravitational waves have been looked for over the past decades, and the sources whose emission if most likely to be picked up are inspiralling close compact systems and mergers of objects like black holes and neutron stars. Recently experimental effort has gone into the development of large scale laser interferometric gravitational-wave observatories on ground such as LIGO in Washington and MiniGRAIL in Leiden (Netherlands) and in space such as the proposed LISA mission. Meanwhile theoretical activity in the field has focused on obtaining accurate predictions of the gravitational wave form signal. There is experimental evidence. Orbital decay due to the emission of gravitational waves has been detected. Its amount is estimated to agree with general relativity to better than half a percent using the Hulse–Taylor binary pulsar, [Weisberg and Taylor, 2005]. Other binary pulsar systems have yielded other tests, especially of strong-field effects. Will [2011] points out that the post-Newtonian approximation, presented in section 3.2.1, has been shown to be "unreasonably effective" for extreme conditions such as mergers of compact objects. When direct observation of gravitational radiation from astrophysical sources begins, new tests of general relativity will be possible.

3.2 Equations for light propagation in the post-Newtonian limit

The pivotal point in astrometry is stressed by [Bastian, 2007](section 4.2.1.3, p. 22):

> *The primary quantity to be measured is the direction of light rays. This quantity also can be expressed in the ICRS by spherical longitude and latitude coordinates (α) and (δ), or else by Cartesian unit vectors. Conceptually, however, it should not be mixed up with the BCRS coordinates of the corresponding body from which the light ray originated. Light rays are curved, and the observed direction of a light ray depends on the point of observation and on the motion of the observer.*

This sums up two essential features in relativistic astrometry: that the geometry of space has to be taken into account and that the motion of the observer has to be accounted for. Both are crucial to making the best use of Gaia data.

What is needed to achieve this is a metric theory of gravity and a set of frames, coordinates and data about the physical universe (mass distributions) to provide a model for light propagation. Several different approaches to this problem exist and have been outlined in Klioner [2003] , Crosta and Mignard [2006], Kopeikin and Makarov [2007] and Crosta [2010].

In this study of light deflection by Jupiter we have followed the model presented in Crosta and Mignard [2006] and implemented it for calculations in AGISLab.

In this section, we will present the main results of the post-Newtonian approximation useful in our calculation. Here PPN γ will make its appearance to quantify the possible deviations of physical universe from general relativity. We then present the model used for the planet (multipole expansion) and then the equations derived in Crosta and Mignard [2006] as well as the derivation of a quantity needed for calculations in AGISLab.

3.2.1 The post-Newtonian limit for theories of gravitation

We outline how the post-Newtonian Limit of a gravitational theory is obtained. [Will, 1993] gives a detailed overview covering the procedure for different kinds of theories in chapter 5. We will discuss the main steps and then go on to the post-Newtonian equations of light bending we study here.

The field equations of general relativity : (2) are elegant and deceptively simple, showing how geometry is generated by matter.

$$G_{\mu\nu} = \frac{8\pi G}{c^4} T_{\mu\nu} \tag{2}$$

$$\left(-\partial^2_{ct} + \nabla^2 \right) h^{\alpha\beta} = -\frac{16\pi G}{c^4} \tau^{\alpha\beta} \tag{3}$$

Where $G_{\mu\nu}$ is the Einstein tensor which is a function of the components of the metric ($g_{\alpha\beta}$), its first derivatives and its second derivatives. For a given material energy-momentum tensor $T_{\mu\nu}$, (2) are second order differential equations constraining the metric, and thereby defining the geometry of space-time. [7] The constant G is Newton's constant of gravitation and c is the speed of light in vacuum, their units are discussed in appendix C. The quantity $8\pi G/c^4 = 2.07 * 10^{-43}[\mathrm{s}^2\mathrm{m}^{-1}\mathrm{kg}^{-1}]$ is called Einstein's constant of gravitation.

The space-time metric being $g_{\alpha\beta}$ and $g = \det(g_{\alpha\beta})$. The tensor $h_{\alpha\beta}$ in (3) is used in the post-Newtonian approximation. It quantifies the deviation of the metric from the flat Minkowski metric which is ($\eta_{\alpha\beta}$):

$$h^{\alpha\beta} = \eta^{\alpha\beta} - (-g)^{1/2} g^{\alpha\beta}. \tag{4}$$

The "relaxed" Einstein equations (3) are employed in post-Newtonian calculations. Will in Will [2011] calls $\tau^{\alpha\beta}$ the "effective" energy-momentum pseudotensor. It can be directly seen that (3) are a second order differential equations.

[7] The Einstein tensor is a function of the Riemann curvature tensor. Definitions are given in appendix B.

The post-Newtonian approximation supposes that gravitational fields are weak and that characteristic motions of matter are slow compared to the speed of light. As pointed out by Will [2011], this means that for the system in question the quantity $\varepsilon \sim (v/c)^2 \sim GM/(Rc^2) \rightsquigarrow 0$ is small. Here v, M, R denote the characteristic velocity, mass, and distance within the system. He stresses that it is unkown whether the post-Newtonian expansion forms a convergent series.

In brief the steps to calculate the post-Newtonian limit of a metric theory of gravitation according to [Will, 1993](chapter 5) are shown in table 1.

step 1:	identify the variables of the theory
step 2:	set cosmological boundary conditions
step 3:	expand in a post-Newtonian series about asymptotic values
step 4:	substitute into field equations
step 5:	solve for the metric element h_{00} to second order
step 6:	solve for the metric elements h_{ij} to second order and solve for h_{0j} to third order
step 7:	solve for the metric elements h_{00} to fourth order. (Will mentions that this is the biggest step and involves the non-linearities of the theory.)
step 8:	convert to local quasi-cartesian coordinates and standard PPN gauge
step 9:	comparison with a reference "shape" of the equations to read of the values of the parameters

Table 1: Procedure to deduce the post-Newtonian limit of a metric theory of gravitation according to [Will, 1993](chapter 5).

The values of the PPN parameters for general relativity, as given in Will [2006, table 2, p.29]:

$$\begin{aligned} \gamma \;=\; \beta \;&= 1 \\ \xi \;&= 0 \\ \alpha_1 = \alpha_2 = \alpha_3 \;&= 0 \\ \zeta_1 = \zeta_2 = \zeta_3 = \zeta_4 \;&= 0 \end{aligned}$$

We note that general relativity is a fully conservative theory, as a consequence of $\alpha_i = 0$ and $\zeta_i = 0$, without preferred frame effects ($\alpha_i = 0$). For alternative theories these parameters will depend on its fundamental scalar and vector fields.

3.2.2 Equations of light propagation

Our goal is to compare the difference in light deflection effects predicted by alternative theories of gravitation in the post-Newtonian limit. This case is relevant for observations of light deflection by the giant planets of the solar system with Gaia. We denote the coordinates x^β, with Greek indices ranging form 0 to 3.

In the limit of geometrical optics, that is when the wave length of the electromagnetic wave of our light ray is small compared with the scale at which its amplitude changes and the scale at which the background geometry changes, we have along the light path:

$$g_{\alpha\beta}\partial_\lambda x^\alpha \partial_\lambda x^\beta \;=\; 0 \tag{5}$$

$$\partial_\lambda x^\alpha \left(\partial_\lambda x^\beta\right)_{;\alpha} \;=\; 0 \tag{6}$$

This is the geodetic equation for a light ray. As discussed in Will [1993, equation (6.7)],where λ is the "affine" parameter measuring the length along the light path. $A_{;\alpha}$ denotes the covariant derivative of A. The first relation (5) shows that the trajectory of the light ray is a null-geodesic. The equation (6) leads to (7), where Gamma is the Christoffel symbol:

$$\partial^2_\lambda x^\mu + \Gamma^\mu_{\alpha\beta}\partial_\lambda x^\alpha \partial_\lambda x^\beta \;=\; 0 \tag{7}$$

From which one can deduce, by applying the post-Newtonian approximation and the parametrized post-Newtonian framework:

$$\frac{d^2x^j}{dt^2} = \partial_j U \left(1 + \gamma\, \delta_{ik} \frac{dx^i}{dt}\frac{dx^k}{dt} \right) - 2(1+\gamma) \frac{dx^j}{dt} \left(\delta_{ik} \frac{dx^i}{dt}\, \partial_k U \right) \tag{8}$$

Where U is an arbitrary gravitational potential satisfying conditions discussed in the next section (3.2.3) and δ_{ij} is the Kronecker delta. This is expression (1) used by Crosta and Mignard [2006].

3.2.3 The multipole expansion

In this section we discuss the gravitational potential we use. This is part of the modeling of the light deflection problem as discussed above. A potential is needed for equation (19). The shape of the potential determines the effects which can be obtained from it. The expression, valid in any coordinate system, for the gravitational potential of a given mass distribution described by a density ρ is :

$$U(\mathbf{x}, t) = \int_B d^3r\, \frac{G\rho(\mathbf{r}, t)}{||\mathbf{x} - \mathbf{r}||} \tag{9}$$

where $\mathbf{x} = (x^1, x^2, x^3)$ is the coordinate three vector of the point at which we compute the potential, $\mathbf{r}$ is the coordinate three vector of integration and B designates the volume occupied by the mass distribution, which may depend on time. The density ρ measures the rest-mass density in a local freely falling frame momentarily comoving with the gravitating matter.

Since our objective is to calculate the gravitational potential of a giant gaseous planet the multipole expansion is a useful tool in simplifying expression (9). It is obtained by Taylor expansion of the norm $||\mathbf{x} - \mathbf{r}||$:

$$\frac{1}{||\mathbf{x} - \mathbf{r}||} = \left(\mathbf{x}^2 - 2\mathbf{x}\cdot\mathbf{r} + \mathbf{r}^2 \right)^{-1/2} = \frac{1}{x} \sum_{n=0}^{\infty} \left(\frac{r}{x} \right)^n P_n\left(\cos(\chi) \right) \tag{10}$$

where χ is the angle between $\mathbf{r}$ and $\mathbf{x}$. Their respective norms are denoted by r and x. In the series expansion (10) the P_n are Legendre polynomials[8]. They are further discussed in appendix D. The series is convergent for all $\mathbf{x}$ such that $r < x$, therefore it does converge if $\mathbf{x}$ is outside a sphere containing the body. This is a classical result of the theory of spherical harmonics (Landau and Lifshitz [1975] §41).

The potential can now be written as :

$$U(\mathbf{x}, t) = \int_B d^3r\, \frac{G\rho(\mathbf{r}, t)}{x} \sum_{n=0}^{\infty} \left(\frac{r}{x} \right)^n P_n\left(\cos(\chi) \right) \tag{11}$$

$$= \frac{G}{x} \sum_{n=0}^{\infty} \left(\frac{1}{x} \right)^n \int_B d^3r\, \rho(\mathbf{r}, t) r^n\, P_n\left(\cos(\chi) \right) \tag{12}$$

$$= \frac{GM}{x} + \frac{G\,\mathbf{p}\cdot\mathbf{x}}{x^3} + \frac{G}{2}\frac{\mathbf{Q_{ij}x_i x_j}}{x^5} + \dots \tag{13}$$

In the above terms of higher order than quadrupole have been neglected. We denote the total mass of the distribution by M.

The dipole moment of the mass distribution is given by (14).

$$\mathbf{p}(t) = \int_B d^3x\, \rho(\mathbf{x}, t)\, \mathbf{x} \tag{14}$$

[8]The Legendre polynomials were introduced in 1782 by Adrien-Marie Legendre for exactly this expansion of the Newtonian potential. [Le Gendre, 1782]

In the planet's proper frame, it vanishes if the mass distribution has a center of symmetry, since all masses are positive and the symmetry entails that the integrand is an uneven function. This is a very good approximation for a planet like Jupiter.

The quadrupole moment of the mass distribution is given by (15), it is a symmetric trace free tensor of rank 2.

$$Q_{ij}(t) = \int_B d^3x\, \rho(\mathbf{x}, t) \left(x_i x_j - \frac{1}{3}\delta_{ij} r^2 \right)$$

To a very good approximation, planets are spherical and they are cylindrically symmetric around their axis of rotation. This shape can be accounted for to reasonably good approximation by the monopole and quadrupole terms in the expansion. The latter accounts for the flattening at the poles as a deviation from spherical shape. Since Q_{ij} is a symmetric real valued tensor it can be brought to principal axes. One of these is the axis of rotation of the planet $\mathbf{z}$, which is also a symmetry axis. The principal value associated with this axis shall be denoted by J_2, then the other two principal values I_1, I_2 associated to axis in the x, y plane are equal, since Q is trace free : $I_1 = I_2 = -1/2\, J_2$.

With these assumptions the potential can be written as :

$$U(\mathbf{x}, t) = \frac{GM}{x} + \frac{G}{2} \frac{Q_{il} x_i x_l}{x^5} + \dots \tag{15}$$

$$\Rightarrow \quad \partial_j U(\mathbf{x}, t) = GM\, \partial_j \frac{1}{x} + \frac{G}{2}\, \partial_j \left(\frac{Q_{il} x_i x_l}{x^5} \right) \tag{16}$$

The gradient $\partial_j U$ of the potential, is used in the formulae for quadrupole light deflection.

Jupiter is the most massive planet in the Solar System and has the largest radius also. A selection of physical data relevant to our experiment is presented in table 2. In the context of light deflection, Jupiter is heavy enough to create observable monopole light deflection. Its quadrupole moment is also large enough for the quadrupole deflection to reach 240 arcsec at its limb (table 1 p. 1588 [Klioner, 2003]). To compute the quadrupole term the direction of Jupiter's rotation axis must be known. In the present work we will assume that it is orthogonal to Jupiter's orbital plane, more sophisticated models have been discussed by the REMAT group Lattanzi and Crosta [2009].

Partly due to its size it is a very bright object ($V \approx -2.7$), this is far below the magnitude threshold of $G = 5.7$ mag, even accounting for the correction of $V \to G$ [Martin Fleitas et al., 2011]. For this reason it cannot directly be observed by Gaia and observations in its vicinity may be impaired [ibidem].

Quantity	Symbol	Unit	Value
radius mean	R_J	$[km]$	$69\,911 \pm 6$
— mean equatorial	R_{Jme}	$[km]$	$71\,492 \pm 4$
mass	M_J	$[10^{24}\,kg]$	1898.13 ± 19
density	ρ_J	$[g\,cm^{-3}]$	1.3262 ± 0.0004
quadrupole moment †	J_2	[1]	$14.7 * 10^{-3}$
period, orbital	T	[yr]	11.862615
— spin	S	[day]	0.41354
magnitude *	V	[mag]	-2.70
grazing ray deflection (monopole)[9]	$\delta\phi$	[arcsec]	0.0163

Table 2: Physical parameters for Jupiter provided by JPL : `http://ssd.jpl.nasa.gov/?planet_phys_par`. († The value for the quadrupole moment J_2 is taken from Fienga et al. [2008] as cited by Zschocke and Klioner [2011]. * The value for V is taken from Martin Fleitas et al. [2011].)

Figure 10: A picture of Jupiter in the visible taken by the Cassini probe. (Credit: NASA/JPL/Space Science Institute; PIA04866)

[9]Calculated using the formula 28, for an observer on Earth or for Gaia's orbit (for the point of closest approach of Jupiter and the observer). Klioner [2003] gives 1620 μarcsecfor monopole deflection by Jupiter

3.2.4 Transformations of the source direction

The source direction is the direction from the observer towards the source, it can be expressed in different reference systems. The source direction undergoes transformations as outlined in Lindegren et al. [1992] and Klioner [2008].

At a given time a star in the Milky Way has a definite position in the BCRS. This direction is defined by the source's astrometric parameters, which to obtain with great accuracy is the point of astrometry. We here study the extent to which light deflection, in particular monopole and quadrupole contributions affect measurement of stellar positions for the Gaia space mission.

The (BCRS) coordinate direction of a sources is the (apparent) Euclidean (3-vector) direction from the barycenter of the Solar System toward the source. It is expressed in the locally Euclidean (or Minkowskian) reference frame of an observer at the barycenter. The notation for it is $\bar{\mathbf{u}}$. It is obtained from the (BCRS) barycentric astrometric parameters of the object by taking into account transformations for secular acceleration, proper motion and parallax.

The natural direction is $\hat{\mathbf{u}}$. It is the direction from a hypothetical observer, who is stationary in BCRS. The transformation from the coordinate direction to the natural direction accounts for the shift of origin from the barycenter of the Solar System to the position of the observer. That is the origin of the natural frame of the satellite (SRS). This vector is obtained by accounting for light deflection ($\Delta\Phi$) by the sun and planets, notably Earth and Jupiter. This term will be considered in the next section 3.2.6. The transformation from $\bar{\mathbf{u}}$ to $\hat{\mathbf{u}}$ is given by:

$$\hat{\mathbf{u}} \quad = \quad \langle\, \bar{\mathbf{u}} + \Delta\Phi \,\rangle = \frac{\bar{\mathbf{u}} + \Delta\Phi}{||\, \bar{\mathbf{u}} + \Delta\Phi \,||} \tag{17}$$

The observable or "proper" direction of a source is denoted $\mathbf{u}$. For Gaia it is the source direction expressed in the CoMRS frame. It is obtained by carrying out the Lorentz transformation accounting for the observer's motion in BCRS. This means that, it is obtained from the natural direction by accounting for stellar aberration due to the barycentric velocity ($\mathbf{v}$) of the satellite.

$$\mathbf{u} \quad = \quad \left\langle\, \hat{\mathbf{u}} + \mathbf{v}\frac{1 + \hat{\mathbf{u}} \cdot \mathbf{v}(c+e)^{-1}}{e} \,\right\rangle \tag{18}$$

where $e = (c^2 - ||\mathbf{v}||^2)^{1/2}$. These equations (17 and 18) are taken from section 5.2 of Lindegren [2001].

3.2.5 Equations of quadrupole light deflection

The differential equations of the null-geodesic light path in the post-Newtonian approximation are (19). The potential and its gradient derived in the previous section are then used to solve them. For a given observed star position, the equations allow to trace the light path back to emission event, that is the location of the source at the moment of emission. For the configurations and bodies we study, the gravitational fields are weak and therefore the "deflection" effect is small. We will calculate the deflection vector of the light path $\Delta\Phi$, its magnitude can be interpreted as the deflection angle. We use the ICRS frame (also called E in Gaia notation), to define vectors. It is a local quasi Cartesian coordinate system [Will, 1993, p. 92].

We discuss the equations given in Crosta and Mignard [2006]. The notation has been adapted to AGISLab notation. Stars will be referred to as "sources". We use the right-handed basis $\mathbf{n}, \mathbf{t}, \mathbf{m}$ which is defined by the light ray arriving from the source as seen in figure 11. The tangent vector to the ray is $\mathbf{t}$, the vector $\mathbf{n}$ points towards the planet along the impact parameter b and $\mathbf{m} = \mathbf{n}\times\mathbf{t}$. The notation for the spin axis of the planet is $\mathbf{z}$. The direction from the observer to the planet is $\mathbf{u}_{\mathrm{p}}$. Crosta and Mignard suppose that the planets are "isolated stationary axisymmetric masses". Hence the formulae we give below are valid in Jupiter's rest frame.

For a light ray passing outside the matter distribution, Crosta and Mignard integrate the following equation:

$$\partial_t^2 x^j_{D\perp} = (1+\gamma)\nabla_\perp U \tag{19}$$

where x^j_D is the relativistic deviation to the zero order (Newtonian) straight line trajectory, and $\nabla_\perp U$ is the projection of the gradient of U (16) onto the plane perpendicular to the light ray. This is the $(\mathbf{n}, \mathbf{m})$ plane shown in figure 11 (b).

The light deflection of the ray is obtained as:

$$\Delta\Phi = \int_{path} \partial_l \mathbf{t}\, dl = \int_{path} (1+\gamma)\nabla_\perp U\, dl \tag{20}$$

with the following expression for the gradient:

$$\begin{aligned} \nabla_\perp U \;=\; & \left[-\frac{b}{r}\left(-\frac{M}{r^2} + \frac{3M}{r^4}\, J_2 R^2\, \frac{5\cos^2(\chi)-1}{2} \right) - \frac{3M}{r^4}\, J_2 R^2\, \cos(\chi)\, (\mathbf{z}\cdot\mathbf{n}) \right] \mathbf{n} \\ & - \frac{3M}{r^4}\, J_2 R^2\, \cos(\chi)\, (\mathbf{z}\cdot\mathbf{m})\, \mathbf{m} \end{aligned} \tag{21}$$

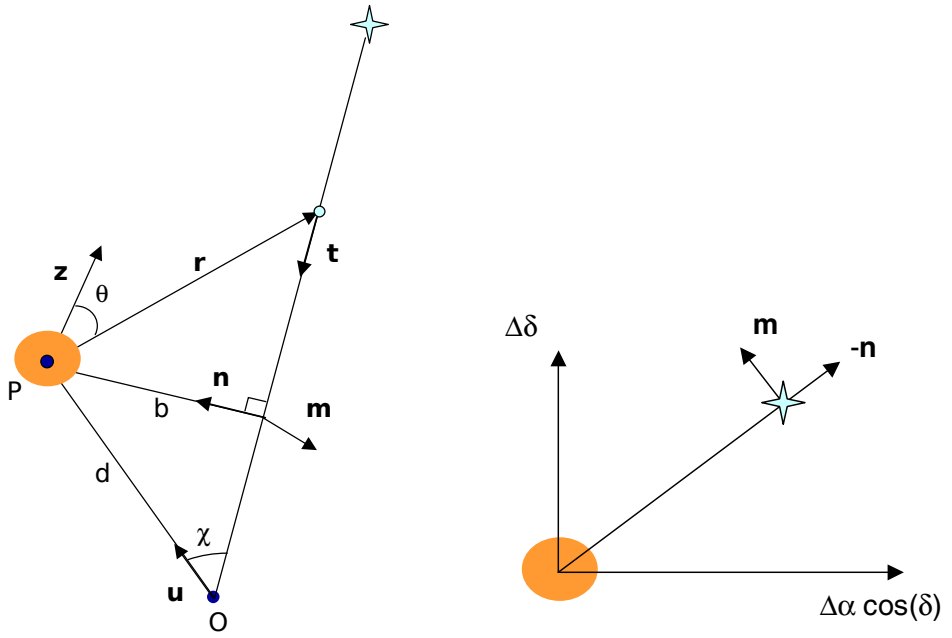

(a) The geometry of light deflection due to a planet (P): the spin axis of the planet **z** is out of the plane; **t** represents the unit tangent vector from a distant star (S) to the observer (O) on the unperturbed light trajectory; **u** is the unit direction from O to P along their distance d ; finally, χ is the angle $\widehat{SOP}$, and b is the impact parameter.

(b) Light deflection by a planet: tangent plane on the sky. The position of the star is displaced both in the radial ($-\mathbf{n}$) and orthoradial **m** directions. The spin axis of the planet **z** (not shown here) does not lie in this plane in general.

Figure 11: Figures describing the light deflection geometry from Crosta and Mignard [2006]

Upon integration of equation (20) along the *path* from the source to the observer the projection of the deflection vector onto the $(\mathbf{n}, \mathbf{m})$ plane is obtained. For its components Crosta and Mignard [2006] obtain:

$$\Delta\Phi = \Delta\Phi_1\,\mathbf{n} + \Delta\Phi_2\,\mathbf{m} \tag{22}$$

$$\begin{aligned}\Delta\Phi_1 = {} & (1+\gamma)\,\frac{GM}{c^2}\,\frac{1}{ab}\left((1+\cos\chi) + J_2\,\frac{R^2}{a^2b^2}\left[\;(1+\cos\chi+\frac{1}{2}\cos\chi\sin^2\chi)\right.\right.\\ & -2\,(1+\cos\chi+\frac{1}{2}\cos\chi\sin^2\chi+\frac{3}{4}\cos\chi\sin^4\chi)(\mathbf{n}\cdot\mathbf{z})^2\\ & +(\sin^3\chi-3\sin^5\chi)(\mathbf{n}\cdot\mathbf{z})(\mathbf{t}\cdot\mathbf{z})\\ & \left.\left.-(1+\cos\chi+\frac{1}{2}\cos\chi\sin^2\chi-\frac{3}{2}\cos\chi\sin^4\chi)(\mathbf{t}\cdot\mathbf{z})^2\;\right]\right)\end{aligned} \tag{23}$$

$$\begin{aligned}\Delta\Phi_2 = {} & (1+\gamma)\,\frac{GM}{c^2}\,J_2\,\frac{R^2}{a^3b^3}\left(\;2(1+\cos\chi+\frac{1}{2}\cos\chi\sin^2\chi)\;(\mathbf{n}\cdot\mathbf{z})\;(\mathbf{m}\cdot\mathbf{z})\right.\\ & \left.+\sin^3\chi\;(\mathbf{m}\cdot\mathbf{z})\;(\mathbf{t}\cdot\mathbf{z})\;\right)\end{aligned} \tag{24}$$

The parameters in this formula are :

- R is the equatorial radius of the deflecting object, M its mass and J_2 the quadrupole moment.
- where d as shown in figure 11 (a) is the distance from Gaia to the deflecting object, measured in astronomical units (AU)

- b is the impact parameter, the distance from the planet to the trajectory of the light ray, it is also measured in AU. We have: $b = d\sin(\chi)$
- χ if the angle between the directions from the observer toward the source and the planet, we have $\chi = (\widehat{\mathbf{u}_\mathrm{p}, -\mathbf{t}})$ and $\cos(\chi) = -(\mathbf{u}_\mathrm{p} \cdot \mathbf{t})$.
- a is the value of 1 AU in meters as given in table 6 in appendix C.

An interesting particular case of formula (22) is the limit $J_2 \to 0$.

$$\Delta\Phi_1 \;\to\; (1+\gamma)\,\frac{GM}{c^2}\,\frac{1}{ab}\,(1+\cos\chi) \tag{25}$$

$$\Delta\Phi_2 \;\to\; 0 \tag{26}$$

$$\Rightarrow \Delta\Phi \;\to\; (1+\gamma)\,\frac{GM}{c^2}\,\frac{1}{ab}\,(1+\cos\chi)\,\mathbf{n} \;=\; (1+\gamma)\,\frac{GM}{c^2}\,\frac{1}{ad}\left(\frac{1+\cos\chi}{\sin\chi}\right)\mathbf{n} \tag{27}$$

We obtain the expected equation for the monopole light deflection:

$$||\Delta\Phi|| \to \delta_m\phi = (1+\gamma)\,\frac{GM}{c^2 ad}\left(\frac{1+\cos\chi}{\sin\chi}\right) = (1+\gamma)\,\frac{GM}{c^2 ad}\,\mathrm{cotan}\left(\frac{\chi}{2}\right) \tag{28}$$

The monopole deflection angle $\delta_m\phi$ (with $\gamma = 1$) was used by Eddington for the solar light deflection experiment to confirm general relativity. Its value is 1.75 arcsec for grazing rays. The formula was also used in Hipparcos data reduction for light deflection by the Sun and Earth [Lindegren et al., 1992].

In the following we call quadrupole term the quantity: $\Delta_q\Phi = (\Delta\Phi_1 - \delta_m\phi)\,\mathbf{n} + \Delta\Phi_2\,\mathbf{m}$.

3.2.6 The quadrupole efficiency factor and derivatives

A further equation is needed for numerical resolution of the quadrupole light deflection equations in the AGIS framework. Therefore we introduce the quadrupole efficiency factor and deduce equations (34) and (35). We then obtain the equation (47) for the derivatives of the source direction vector, as required by the AGIS scheme. This refers to the method outlined in section 4.1 of report 2.

The formulae (23) and (24) being heavy, we introduce the following notation:

$$\mathcal{A} \;=\; (1+\gamma)\,\frac{GM}{c^2}\,\frac{1}{ab} \tag{29}$$

$$\mathcal{B} \;=\; J_2\,\frac{R^2}{a^2b^2} \tag{30}$$

$$\mathcal{C} \;=\; \frac{GM}{c^2}\,\frac{1}{a^2d^2}\,\frac{1}{1-\cos(\chi)} \tag{31}$$

$$\begin{aligned} f_1(\chi) \;=\;& (1+\cos\chi+\frac{1}{2}\cos\chi\sin^2\chi) \\ & -2\,(1+\cos\chi+\frac{1}{2}\cos\chi\sin^2\chi+\frac{3}{4}\cos\chi\sin^4\chi)(\mathbf{n}\cdot\mathbf{z})^2 \\ & +(\sin^3\chi-3\sin^5\chi)(\mathbf{n}\cdot\mathbf{z})(\mathbf{t}\cdot\mathbf{z}) \\ & -(1+\cos\chi+\frac{1}{2}\cos\chi\sin^2\chi-\frac{3}{2}\cos\chi\sin^4\chi)(\mathbf{t}\cdot\mathbf{z})^2 \end{aligned} \tag{32}$$

$$\begin{aligned} f_2(\chi) \;=\;& 2(1+\cos\chi+\frac{1}{2}\cos\chi\sin^2\chi)\;(\mathbf{n}\cdot\mathbf{z})\;(\mathbf{m}\cdot\mathbf{z}) \\ & +\sin^3\chi\;(\mathbf{m}\cdot\mathbf{z})\;(\mathbf{t}\cdot\mathbf{z}) \end{aligned} \tag{33}$$

The quadrupole efficiency factor (QEF) is denoted by ε, as in [Crosta and Mignard, 2006]. It scales the quadrupole term in equations (23) and (24). These equations become:

$$\Delta\Phi_1 = \mathcal{A}\ [\ (1+\cos\chi)\ +\ \varepsilon\,\mathcal{B}\ f_1(\chi)\ ] \tag{34}$$
$$\Delta\Phi_2 = \varepsilon\,\mathcal{A}\,\mathcal{B}\ f_2(\chi) \tag{35}$$

Equation (22) still holds, the total deflection is $\Delta\Phi = \Delta\Phi_1\,\mathbf{n} + \Delta\Phi_2\,\mathbf{m}$.

The derivatives required by the AGIS framework are those of the natural source direction $\hat{\mathbf{u}}$ with respect to ε. Here we give the detail of their calculation.

$$\frac{\partial\,\hat{\mathbf{u}}}{\partial\varepsilon} = \partial_\varepsilon\,\hat{\mathbf{u}} \tag{36}$$
$$= \frac{\partial_\varepsilon\Delta\Phi}{||\ \bar{\mathbf{u}}+\Delta\Phi\ ||}\ +\ (\bar{\mathbf{u}}+\Delta\Phi)\ \partial_\varepsilon\left(\frac{1}{||\ \bar{\mathbf{u}}+\Delta\Phi\ ||}\right) \tag{37}$$
$$= \frac{(\ \partial_\varepsilon\Delta\Phi_1\ )\ \mathbf{n} + (\ \partial_\varepsilon\Delta\Phi_2\ )\ \mathbf{m}}{||\ \bar{\mathbf{u}}+\Delta\Phi\ ||}\ +\ (\bar{\mathbf{u}}+\Delta\Phi)\ \partial_\varepsilon\left(\frac{1}{||\ \bar{\mathbf{u}}+\Delta\Phi\ ||}\right) \tag{38}$$

Where we use the notation: $\partial_x = \frac{\partial}{\partial x}$. It follows:

$$\partial_\varepsilon\Delta\Phi = (\ \partial_\varepsilon\Delta\Phi_1\ )\ \mathbf{n} + (\ \partial_\varepsilon\Delta\Phi_2\ )\ \mathbf{m} = \mathcal{A}\,\mathcal{B}\ f_1(\chi)\mathbf{n}\ +\ \mathcal{A}\,\mathcal{B}\ f_2(\chi)\mathbf{m} \tag{39}$$

$$\partial_\varepsilon\left(\frac{1}{||\ \bar{\mathbf{u}}+\Delta\Phi\ ||}\right) = -\left(\frac{1}{||\ \bar{\mathbf{u}}+\Delta\Phi\ ||^2}\right)\ \partial_\varepsilon\,||\ \bar{\mathbf{u}}+\Delta\Phi\ || \tag{40}$$

$$||\ \bar{\mathbf{u}}+\Delta\Phi\ || = \sqrt{\bar{\mathbf{u}}^2+\Delta\Phi^2\ +\ 2\ \bar{\mathbf{u}}\cdot\Delta\Phi} \tag{41}$$
$$\partial_\varepsilon||\ \bar{\mathbf{u}}+\Delta\Phi\ || = \frac{1}{2}\ \frac{1}{||\ \bar{\mathbf{u}}+\Delta\Phi\ ||}\left(\partial_\varepsilon\left(\Delta\Phi^2\right)+\partial_\varepsilon\ 2\ \bar{\mathbf{u}}\cdot\Delta\Phi\right) \tag{42}$$
$$\partial_\varepsilon||\ \bar{\mathbf{u}}+\Delta\Phi\ || = \frac{1}{2}\ \frac{1}{||\ \bar{\mathbf{u}}+\Delta\Phi\ ||}\left(\ 2\,\Delta\Phi\cdot\partial_\varepsilon\Delta\Phi+\ 2\,\bar{\mathbf{u}}\cdot\ \partial_\varepsilon\ \Delta\Phi\ \right) \tag{43}$$
$$= \frac{(\bar{\mathbf{u}}+\Delta\Phi)\cdot\partial_\varepsilon\left(\ \Delta\Phi\ \right)}{||\ \bar{\mathbf{u}}+\Delta\Phi\ ||} \tag{44}$$

Thus:

$$\partial_\varepsilon\ \hat{\mathbf{u}} = \frac{\partial_\varepsilon\Delta\Phi}{||\ \bar{\mathbf{u}}+\Delta\Phi\ ||} + (\bar{\mathbf{u}}+\Delta\Phi)\ \partial_\varepsilon\left(\frac{1}{||\ \bar{\mathbf{u}}+\Delta\Phi\ ||}\right) \tag{45}$$
$$= \frac{\partial_\varepsilon\Delta\Phi}{||\ \bar{\mathbf{u}}+\Delta\Phi\ ||}\ +\ (\bar{\mathbf{u}}+\Delta\Phi)\left(\ -\left(\frac{1}{||\ \bar{\mathbf{u}}+\Delta\Phi\ ||^2}\right)\ \frac{(\bar{\mathbf{u}}+\Delta\Phi)\cdot\partial_\varepsilon\left(\ \Delta\Phi\ \right)}{||\ \bar{\mathbf{u}}+\Delta\Phi\ ||}\right) \tag{46}$$

$$\partial_\varepsilon\ \hat{\mathbf{u}} = \frac{\partial_\varepsilon\Delta\Phi}{||\ \bar{\mathbf{u}}+\Delta\Phi\ ||}\ -\ (\bar{\mathbf{u}}+\Delta\Phi)\ \frac{(\bar{\mathbf{u}}+\Delta\Phi)\cdot\partial_\varepsilon\Delta\Phi}{||\ \bar{\mathbf{u}}+\Delta\Phi\ ||^3} \tag{47}$$

This final expression (47), is the analytic formula for the derivative in the case of a single deflecting body. In the case of multiple deflecting bodies their contributions have to be added as: $\hat{\mathbf{u}}' = \bar{\mathbf{u}} + \Sigma_i\Delta\Phi_i$ and every body may have its own QEF ε_i. In the case of solar system objects and the configuration of Gaia which does not observe close to the Sun, it is sufficiently accurate to calculate derivatives in the approximation of a single body, treat each contribution separately since $||\ \bar{\mathbf{u}}+\Sigma_i\Delta\Phi_i\ || \approx ||\ \bar{\mathbf{u}}\ ||$. This discussion is relegated to section **??**.

The analog of (47) for the monopole term and gamma is (48). In which we use the heliocentric position of Gaia $\mathbf{r}$, the notation $\mathbf{u_1} = \bar{\mathbf{u}} + \Delta\Phi$ and $u_1 = ||\ \mathbf{u_1}\ ||$.

Next we compare this expression to a further approximation (49), which was used for the derivatives in PPN γ for Hipparcos Lindegren et al. [1992] and in AGISLab Hobbs et al. [2010].

$$\frac{\partial\,\hat{\mathbf{u}}}{\partial\gamma} \;=\; -\mathcal{C}\,\frac{1}{u_1^3}\,\left(\,(1+\gamma)\,\mathcal{C}\,\mathbf{r}^2+(\mathbf{r}\cdot\mathbf{u})\,\right)\mathbf{u_1}+\frac{1}{u_1}\,\mathcal{C}\,\mathbf{r} \tag{48}$$

$$\frac{\partial\,\hat{\mathbf{u}}}{\partial\gamma} \;\approx\; (\mathbf{r}\;-\;\bar{\mathbf{u}}(\bar{\mathbf{u}}\cdot\mathbf{r}))\,\frac{GMc^{-2}}{r(r+\bar{\mathbf{u}}\cdot\mathbf{r})} \tag{49}$$

In analogy to (49) we would like to write for $\partial_\varepsilon\,\hat{\mathbf{u}}$:

$$\partial_\varepsilon\,\hat{\mathbf{u}} \;=\; \partial_\varepsilon\Delta\Phi\;-\;(\bar{\mathbf{u}}+\Delta\Phi)\,\partial_\varepsilon(\bar{\mathbf{u}}\cdot\Delta\Phi) \tag{50}$$

The derivation of equation (49) uses Taylor expansions. Knowing that the deflection term $\Delta\Phi$ is small (in most observable cases), we can rewrite (17):

$$\begin{aligned}
\hat{\mathbf{u}} \;&=\; \frac{\bar{\mathbf{u}}+\Delta\Phi}{||\;\bar{\mathbf{u}}+\Delta\Phi\;||} && (51)\\
&=\; (\;\bar{\mathbf{u}}+\Delta\Phi\;)\,\left(\,\bar{\mathbf{u}}^2+2\,\bar{\mathbf{u}}\cdot\Delta\Phi+\Delta\Phi^2\,\right)^{-\frac{1}{2}}\\
&=\; (\;\bar{\mathbf{u}}+\Delta\Phi\;)\,(\,1+2\,\bar{\mathbf{u}}\cdot\Delta\Phi+o(||\Delta\Phi||)\,)^{-\frac{1}{2}}\\
&\approx\; (\;\bar{\mathbf{u}}+\Delta\Phi\;)\left(\,1-\frac{1}{2}\,2\,\bar{\mathbf{u}}\cdot\Delta\Phi+o(||\Delta\Phi||)\,\right)\\
&\approx\; \bar{\mathbf{u}}+\Delta\Phi-\bar{\mathbf{u}}\,(\bar{\mathbf{u}}\cdot\Delta\Phi)-\Delta\Phi(\;\bar{\mathbf{u}}\cdot\Delta\Phi)+o(||\Delta\Phi||)\\
&\approx\; \bar{\mathbf{u}}+\Delta\Phi-\bar{\mathbf{u}}\,(\bar{\mathbf{u}}\cdot\Delta\Phi)+o(||\Delta\Phi||)\\
&\approx\; \bar{\mathbf{u}}+(1-\bar{\mathbf{u}}\,\bar{\mathbf{u}}^T)\Delta\Phi+o(||\Delta\Phi||) && (52)
\end{aligned}$$

where $\bar{\mathbf{u}}^2=1$ and $\Delta\Phi(\;\bar{\mathbf{u}}\cdot\Delta\Phi)=o(||\Delta\Phi||)$

Upon deriving (52) with respect to ε:

$$\begin{aligned}
\partial_\varepsilon\,\hat{\mathbf{u}} \;&\approx\; \partial_\varepsilon\bar{\mathbf{u}}+\partial_\varepsilon\,\left(\,(1-\bar{\mathbf{u}}\,\bar{\mathbf{u}}^T)\Delta\Phi\,\right) && (53)\\
&\approx\; 0+(1-\bar{\mathbf{u}}\,\bar{\mathbf{u}}^T)\,\partial_\varepsilon\Delta\Phi\\
\partial_\varepsilon\,\hat{\mathbf{u}} \;&\approx\; (1-\bar{\mathbf{u}}\,\bar{\mathbf{u}}^T)\,\partial_\varepsilon\Delta\Phi && (54)\\
\partial_\varepsilon\,\hat{\mathbf{u}} \;&\approx\; \partial_\varepsilon\Delta\Phi-\bar{\mathbf{u}}\;(\;\bar{\mathbf{u}}\cdot\partial_\varepsilon\Delta\Phi\,) && (55)
\end{aligned}$$

Alternatively, deriving (52) with respect to γ:

$$\begin{aligned}
\partial_\gamma\,\hat{\mathbf{u}} \;&\approx\; \partial_\gamma\bar{\mathbf{u}}+\partial_\gamma\,\left(\,(1-\bar{\mathbf{u}}\,\bar{\mathbf{u}}^T)\Delta\Phi\,\right) && (56)\\
&\approx\; 0+(1-\bar{\mathbf{u}}\,\bar{\mathbf{u}}^T)\,\partial_\gamma\Delta\Phi\\
\partial_\gamma\,\hat{\mathbf{u}} \;&\approx\; (1-\bar{\mathbf{u}}\,\bar{\mathbf{u}}^T)\,\partial_\gamma\Delta\Phi && (57)\\
\partial_\gamma\,\hat{\mathbf{u}} \;&\approx\; \partial_\gamma\Delta\Phi-\bar{\mathbf{u}}\;(\;\bar{\mathbf{u}}\cdot\partial_\gamma\Delta\Phi\,) && (58)
\end{aligned}$$

These different expressions for the derivatives have been implemented and tested in AGISLab. The results of the different formulae are compared in the next section.

4 Simulation and analysis of light deflection

In this section we will discuss the implementation of the quadrupole deflection term in AGISLab and the results we have obtained. We are interested in the constraints Gaia astrometry will place on the PPN parameter γ and the measurement of quadrupole gravitational light deflection. The reason we study Jupiter is that the quadrupole deflection by this planet is supposed to be the strongest in the solar system [Klioner, 2003]. In view of this we have run realistic simulations of the astrometric core solution for the Gaia mission.

In the following sections we will discuss the design and implementation of the deflection calculation. We will also describe the configuration of sources (input data) used for the runs. Thereafter we will discuss the results which we have obtained.

4.1 Design of the implementation in the AGISLab framework

4.1.1 The SourceDirection interface

In search of the astrometric solution AGIS needs to calculate the proper direction. The principle is the same in the scaled AGISLab. One of the steps in the transformation from the coordinate direction to the proper direction is the determination of light deflection. This has been discussed in section 3.3.5 of Ludl [2011]. In AGISLab this is handled by the interface SourceDirection. This interface admits different implementations. In figure 12 the relationship between these classes and the interface are depicted.

The first implementation of SourceDirection is SourceDirectionGeometricImpl, written by Hobbs et al. [2010]. This calculates the "proper source direction" starting from observation data. This implementation will be referred to as the "old" model. It was already mentioned in section 3.4.1 of Ludl [2011], that it is based on a model of monopole light deflection for the Sun and planets similar to the one used in Hipparcos data processing [Lindegren et al., 1992]. We will use it as a reference for our simulations when looking at monopole terms and the convergence of PPN γ.

The implementation SourceDirectionGeometricQuadImpl was designed during this project. It takes into account the light deflection terms up to quadrupole order for Jupiter. It can also be used for other planets. It uses the new formalism and derivative equations for PPN γ and the quadrupole efficiency factor (QEF) ε. It implements the validated equations (34) and (35) and the derivatives (47) for QEF ε and (48) for PPN γ. We call this the "new" model. An intermediary version has been implemented and tested for the purpose of comparing results to those of the "old" model. The full quadrupole model is used to study Gaia's ability to detect the so far unobserved quadrupole gravitational light deflection by Jupiter. To this end we simulate the performance of Gaia in realistic simulations including Observation noise and a band of known stars near Jupiter. It will allow direct comparison of our results to those obtained with Gaia's baseline relativity model, GREM, for which SourceDirection will also act as an interface [Klioner, 2003, 2008]. The interface is implemented in SourceDirectionGremImpl as depicted in figure 12.

We have paid attention to writing documentation for the implemented methods. The role of each method is specified, as well as the significance of the input and output parameters. This was done with a view to facilitate testing and subsequent use by the research group.

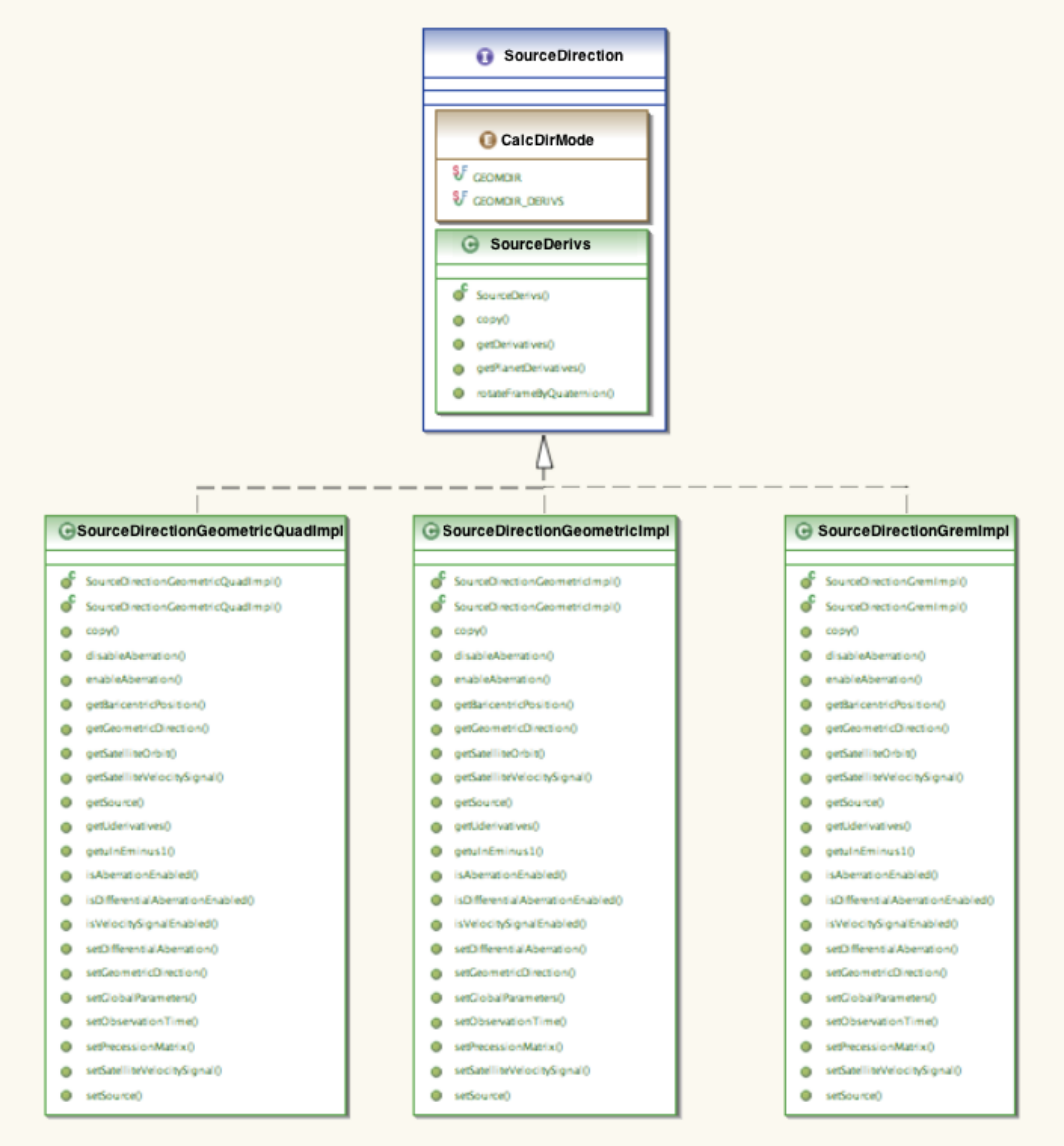

Figure 12: UML diagram depicting the inheritance relationship between SourceDirection, SourceDirectionGeometricImpl, SourceDirectionGeometricQuadImpl and SourceDirectionGremImpl. These classes implement different models for gravitational light deflection. For the former it is the one detailed in this work, the last is based on GREM.

4.1.2 Implementing the source direction calculation

The role of the Global update block in AGIS and AGISLab is to determine the values of a set of model parameters that are constant throughout the mission [Hobbs et al., 2010]. Among those are the PPN γ for the Sun and planets and in addition the quadrupole efficiency factor we have introduced here. The Global update block calculates the updates to the global parameters. It solves the normal equation for the globals, which requires the derivatives of the source direction with respect to the global parameters. This is why we calculate $\partial_\gamma \hat{\mathbf{u}}$ and $\partial_\varepsilon \hat{\mathbf{u}}$ [Hobbs et al., 2010].

The method setObservationTime(GaiaTime, Fov, Quaternion, CalcDirMode) executes the calculation and calls the (private) methods computeMonopoleDeflection(GaiaTime, CalcDirMode) and then computeQuadrupoleDeflection(GaiaTime, CalcDirMode). These evaluate the deflections and derivatives and add the former to the source direction uInE (in E = ICRS). These calculations are implemented in quadrupoleDeflection(GaiaTime, CalcDirMode, int, GVector3d) and monopoleDeflection(GaiaTime, CalcDirMode, int, GVector3d). Their arguments are the time

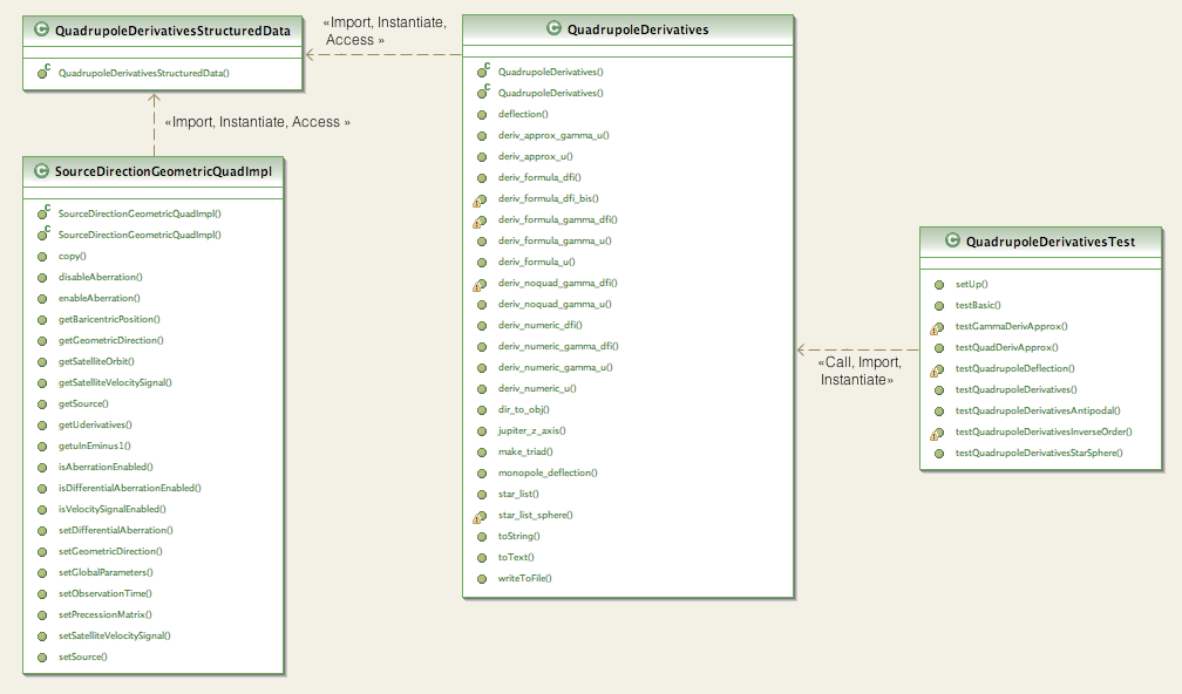

Figure 13: The UML diagram of the relations between the classes SourceDirectionGeometricQuadImpl, QuadrupoleDerivativesStructuredData, QuadrupoleDerivatives and QuadrupoleDerivativesTest. (Also shown in report 1, figure 13)

of the recorded observation event for which the deflection is calculated (GaiaTime), a parameter specifying the calculation mode (CalcDirMode), the integer identifier (int) of the deflecting object (e.g. Jupiter or the Sun) and the position of the deflecting body relative to Gaia in ICRS (GVector3d).

For the design of the methods to be used in SourceDirectionGeometricQuadImpl as described above, we have to split the equations (34) and (35) [Crosta and Mignard, 2006] of the "new" model into monopole and quadrupole terms. The monopole and quadrupole methods for the derivatives respectively calculate (48) for PPN γ and (47) for QEF ε. These equations have been validated as detailed in the previous section 3.4 of Ludl [2011].

The infrastructure required for the representation of relevant quantities was already present in AGISLab. A class representing vectors GVector3d already exists. There are further classes representing Gaia relevant data, such as (SolarSystemEphemeris) and GaiaTime. A few changes had to made to incorporate the global quadrupole efficiency factor (ε) into the global update block. It was necessary to re-factored GlobalTypes and make the changes required for a new parameter in the plotting methods.

To avoid recalculation of terms that will be reused by the methods evaluating the derivatives, the auxiliary class QuadrupoleDerivativesStructuredData has been made a subclass.

4.1.3 The input data

Since our objective is to estimate the accuracy achievable with Gaia for measuring quadrupole light deflection, we chose to use a real star distribution near Jupiter. A list of stars in a band on the sky has been provided by François Mignard in the SOGAR Java bundle. A subset of them have been taken from the Hipparcos and Tycho-2 catalogues.

We used the file listing 2 million stars near Jupiter. Had we used this directly, it would have taken a long time to run a single simulation. Thus we filtered the stars according to magnitude and angular separation to Jupiter. We generated several sets of stars as listed in table 3. The final configuration (set 3) of stars contains all stars which lie within 300 arcsec of Jupiter and are brighter than magnitude 17.

	$\Theta_{\max}$	Magnitude	star number
set 1	300 arcsec	$6 < G < 15$	21 862
set 2	300 arcsec	$6 < G < 15.9$	47 830
set 3	300 arcsec	$6 < G < 17$	74 146

Table 3: The configurations of stars filtered out of the initial file containing 2 million stars. The maximal angular distance form Jupiter $\Theta_{\max}$ and the number of stars in the band, as well as their magnitudes are given. The lower G magnitude limit is 6 since Gaia will not detect brighter stars.

The sources are loaded into AGISLab by implementations of the SourceGenerator interface. The star list does not contain proper motions, therefore we use a random generator to create a realistic distribution. This is done in SourceGeneratorNearJupiterPropMotionImpl. However these stars alone will not permit convergence of AGIS. We have therefore also included a set of randomly generated stars that are uniformly distributed over the sky. This allows the attitude of Gaia to be constrained. For this we use SourceGeneratorRandomImpl. The band of stars of the final configuration is shown in figure 16. Set 1 and 2 were used for quick runs, set 3 for more realistic simulations.

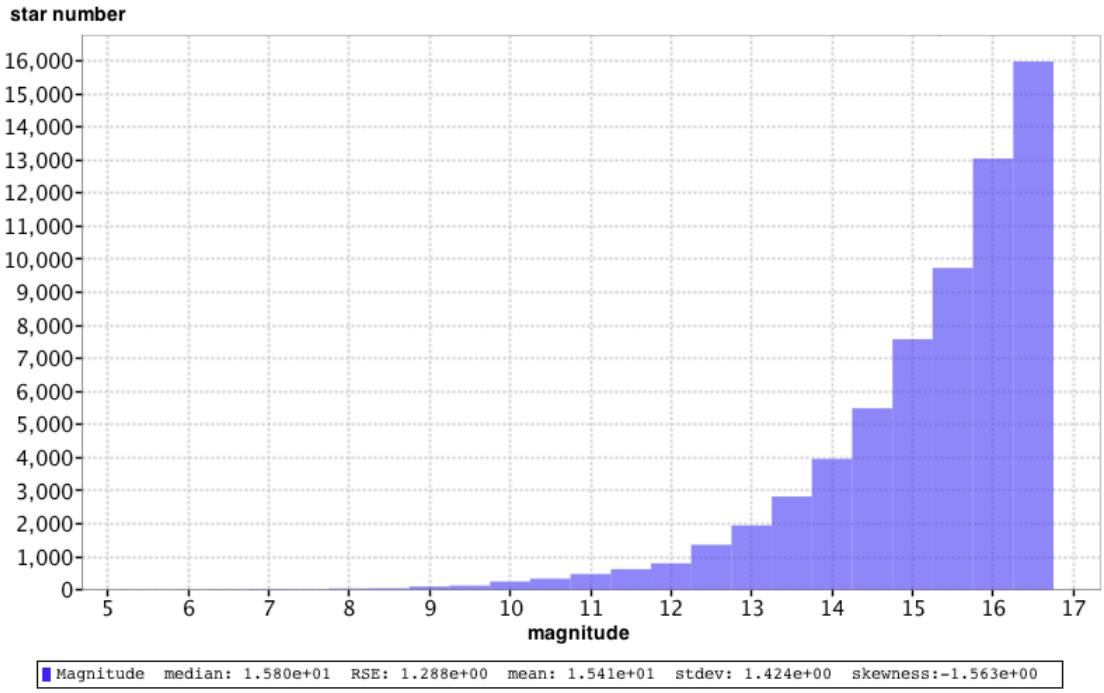

Figure 14: The magnitude distribution of the stars in set 3 (table 3). The statistical characteristics of the data set are indicated below the figure. [image generated with AGISLab]

The model includes Observation noise as described in de Bruijne [2009]. It accounts for the estimated AL and AC location-estimation performance of Gaia. This will be a function of magnitude and affects the weight (w) of each observed star in equation (1).

The noise distribution is Gaussian and depends on the brightness of the sources, thus it produces a spread and noisy observations that have lower weight in equation (1). Thus, for simulations which are otherwise identical, enabling observation noise will result in less good but realistic results.

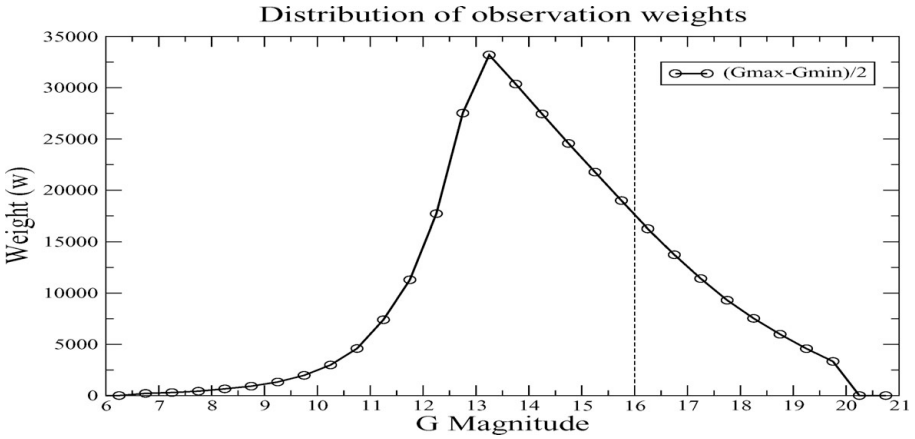

Figure 15: The observation weight distribution as a function of G magnitude, for bins of 0.5 magnitude. (Graph from Hobbs et al. [2010])

We have produced filtered sets of stars to reduce the number of stars so that calculations can be done in a reasonable time (less than a few days) on normal machines. We chose cut offs at magnitudes 15, 15.9 and 17 because the stars with largest weight are stars with G magnitudes lower than 16. This is illustrated in figure 15 which shows the distribution of observation weights. For this reason stars of magnitude $G \leq 16$ provide the largest contribution to the determination of PPN γ [Hobbs et al., 2010]. Nevertheless faint stars provide a contribution as well, for quadrupole simulations we found it necessary to include more stars to constrain the quadrupole efficiency factor.

To correctly account for the quadrupole term, the direction of Jupiter's rotation axis must also be known. In the present implementation, as in report 1, we have assumed that it is orthogonal to Jupiter's orbital plane, more sophisticated models have been discussed by the REMAT group Lattanzi and Crosta [2009].

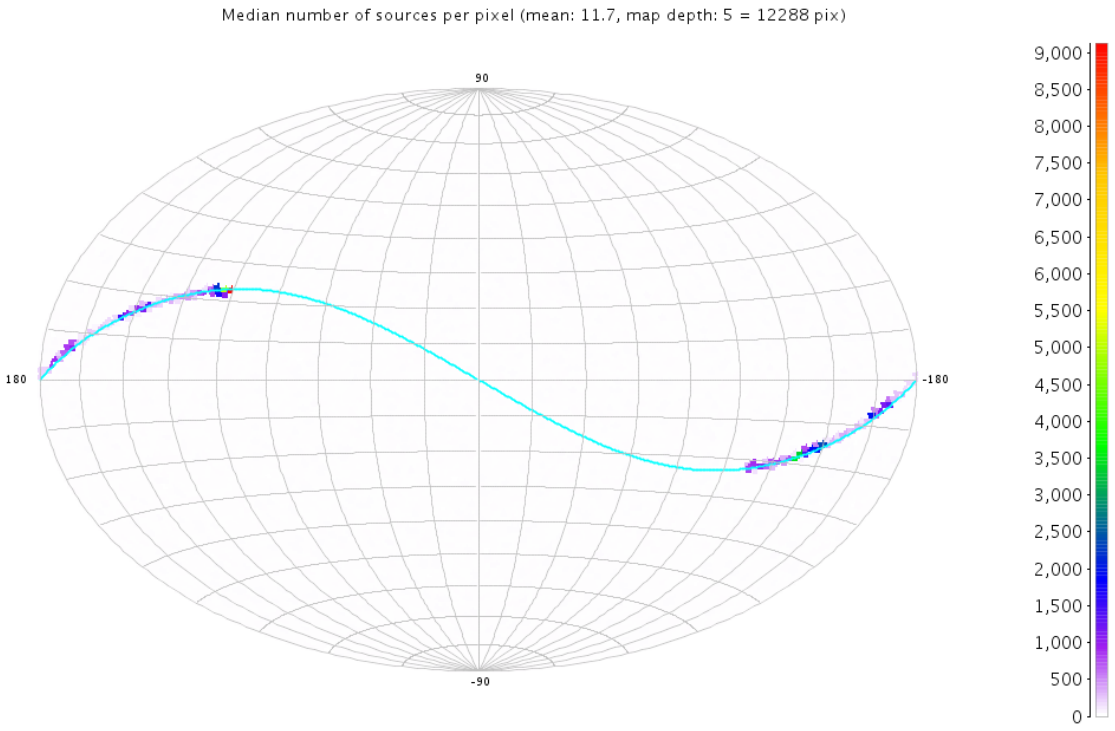

Figure 16: The band of stars near Jupiter used for the simulations of quadrupole light deflection. The squares are color coded to indicate the medium number of sources per pixel, the turquoise line corresponds to the ecliptic. There are 74 146 in a band of width 300 arcsec above and below to Jupiter's trajectory. For the projection the equatorial coordinate system is used. (There are also 70 000 stars all over the sky but their density is much lower than in the band and the automatic color coding in AGISLab has diluted them into white.) [image generated with AGISLab]

4.2 Results and analysis

We discuss the main results of our simulations of quadrupole deflection by Jupiter and the determination of PPN γ using planetary (monopole) light deflection.

4.2.1 A test plan

We have followed the following protocol. First the validity of the implemented equations was tested, this is described in section 3.4 of Ludl [2011]. Then we carried out experiments with relatively small runs using the sets 1 and 2 of stars near Jupiter (table 3). This established the convergence of the implemented formulae and demonstrated the quadrupole term in nearly realistic simulations. Finally we studied the statistical significance of the simulation. In two cases, we performed a set of 10 experiments using different random seeds for random sources, observation noise, this is described below in the respective sections.

There is an analogy between the global parameters PPN γ and QEF ε. For both the baseline model assumes that their value is 1. Hence the errors of the "global parameters" PPN γ for the Sun, PPN γ for Jupiter, and QEF ε for Jupiter, are defined as in equations (65) and (66) in the first report :

$$\begin{aligned} \mathrm{Err}_{\mathrm{Sun}}(\gamma) &= \gamma_S - 1 \\ \mathrm{Err}_{\mathrm{Jup}}(\gamma) &= \gamma_J - 1 \\ \mathrm{Err}_{\mathrm{Jup}}(\varepsilon) &= \varepsilon_J - 1 \end{aligned} \tag{59}$$

case 1	sources observation noise	set 1 and 20 000 random stars Off
case 2	sources observation noise	set 1 and 20 000 random stars On
case 3	sources observation noise	set 3 and 70 000 random stars Off
case 4	sources observation noise	set 3 and 70 000 random stars On

Table 4: The typical configurations for the simulations discussed in this section. For these cases we have performed simulations with and without observation noise and initial errors of source, attitude and global parameters.

4.2.2 Estimates of the achievable accuracy of the measurements for quadrupole deflection by Jupiter

Here we present our results on the estimation of the quadrupole efficiency factor. We analyse the dependence of the standard deviation of QEF ε on the angular width of the exclusion zone around Jupiter.

The exclusion zone is the zone in which observations of stars are impossible. We denote its radius as $\theta_{\text{tot}} = \theta_J + \theta_e$, where θ_J is the angular radius of Jupiter, and θ_e is the angular width of the band where saturation of the CCDs occurs. A technical discussion can be found in [Martin Fleitas et al., 2011], where it is pointed out that in the saturated band false detections occur. In order to avoid false observations, this zone must be filtered out. Martin Fleitas et al. [2011] estimate θ_e to be between 2 and 4 arcsec around Jupiter's limb. We have made simulations in steps of 5 arcsec to study the implications on the observation of quadrupole light deflection.

We have produced simulations using SourceDirectionGeometricQuadImpl, we chose to increment θ_e by steps of 5 arcsec, from 0 arcsec to 20 arcsec.

First we studied the convergence of the new setup. For different values of θ_e we tested different configurations of initial errors of source, attitude and global parameters, and observation noise. In noiseless simulations without initial errors the convergence is very good, in a few iterations $\text{Err}_{\text{Jup}}(\varepsilon)$ reaches a level of 10^{-5}. When observation noise is enabled this value deteriorates to the order of 0.01. As shown for instance in figure 17 (for $\theta_e = 0$ arcsec).

With intial errors in global, source and attitude parameters and observation noise enabled, we obtain an oscillating behaviour as described in section 3.4.3 of Ludl [2011]. This is shown in figure 18. We can see that $\text{Err}_{\text{Jup}}(\varepsilon)$ does converge albeit more slowly.

For a given set of seed parameters, these different runs converge to the same value, but runs with initial errors need more iterations to converge. The converged value of $\text{Err}_{\text{Jup}}(\varepsilon)$ is reasonably small to consider the detectability of the effect.

The second step was then to look at the standard deviations for QEF ε.

The standard deviations have been calculated for simulations of case 4 in table 4. Formal values have been produced with AGISLab, which calculates them at every iteration. We have retained the values of σ_ε at iteration 50. For the square of the standard deviation it uses:

$$\sigma_{g_i}^2 = (N_g^{-1})_{ii} \tag{60}$$

This equation is analogous to equation (3.2) in Holl et al. [2010], where g_i is any global parameter and N_g is the matrix of the global normal equation (90) in Lindegren et al. [2011].

For 0 and 5 arcsec we performed 10 runs each to compute statistically relevant values. Different random seeds for the random sources and observation noise were used. Initial errors were disabled since it does not affect the final value, and convergence can be accelerated in this fashion. Since these Monte Carlo simulations with different seeds are uncorrelated, we can calculate a meaningful average value of (σ_ε) the standard deviations of $\text{Err}_{\text{Jup}}(\varepsilon)$.

A convergence plot is shown in figure 17. In figure 17 we see the convergence for a run with observation noise enabled and 0 arcsec radius of the exclusion zone. This simulation is part of those used to obtain σ_ε for $\theta_e = 0$. The convergence is better than for larger values of θ_e, however the observation noise is propagated and reduces the weight of certain sources. For this reason the converged value of the error ($\text{Err}_{\text{Jup}}(\varepsilon) \approx 0.02$) in this case is larger than for noiseless observations (10^{-5}).

For larger values of θ_e the converged value of the error ($\text{Err}_{\text{Jup}}(\varepsilon)$) is larger because the quadrupole term is weaker at large angles from Jupiter. ($\Delta\Phi \propto 1/b^3$ see section 3.2.5 : equations (22) and (24) and section 3.4.3 of Ludl [2011].

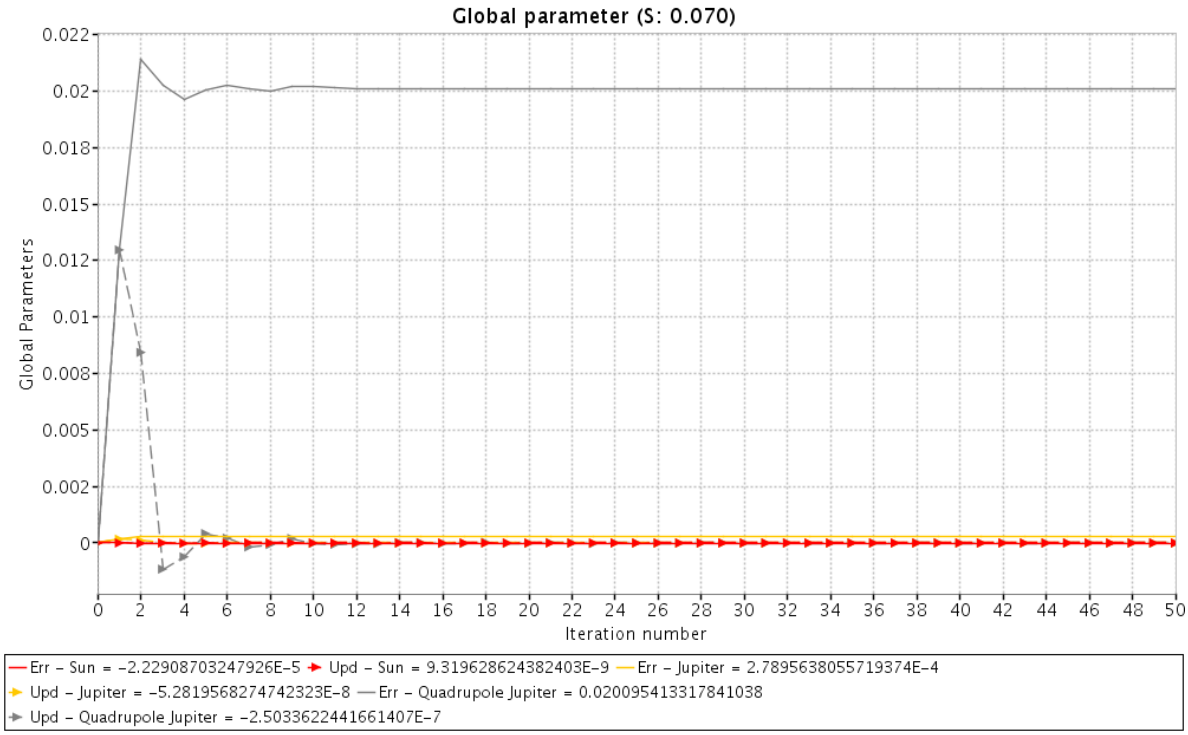

Figure 17: Convergence plot for the global parameters, in red (→) the error in PPN γ of the Sun in yellow (→) the error in PPN γ of Jupiter, and in grey (→) the error in QEF ε of Jupiter. For an exclusion zone radius $\theta_e = 0$ arcsec, no initial errors but observation noise enabled. The numbers in the box at the bottom of the graphs indicate the values at the end of iteration 50. (Plot generated using AGISLab)

The distribution of $\mathrm{Err}_{\mathrm{Jup}}(\varepsilon)$ for ten runs is shown in figure 19 for zero exclusion radius. Most of the error bars for QEF ε do intersect $\mathrm{Err}_{\mathrm{Jup}}(\varepsilon) = 0$. The fact that the distribution is not centered on zero is due to the weakness of the effect and the observation noise. Adding observation noise diminishes the weight of many observations, most stars being faint we effectively lose many observations. This has also been discussed in section 4.1.3. The standard deviations for all runs are very close, their average is $\sigma_\varepsilon = 0.089$. We would expect the average value to be closer to zero if we could solve the astrometric problem exactly.

For the mean value of the errors $\langle\, \mathrm{Err}_{\mathrm{Jup}}(\varepsilon) \,\rangle$ we should have:

$$\left\langle\, \mathrm{Err}^2_{\mathrm{Jup}}(\varepsilon) \,\right\rangle = \left\langle\, (\varepsilon_J - 1)^2 \,\right\rangle \approx \sigma^2_\varepsilon \tag{61}$$

For the data set shown in figure 19 we have : for the formal error $\sigma_\varepsilon = 0.089$ and $\sigma^2_\varepsilon = 0.0079$ as obtained from equation (60). For the average of the errors we have $\left\langle\, \mathrm{Err}^2_{\mathrm{Jup}}(\varepsilon) \,\right\rangle = 0.0099$. These values agree reasonably well considering that we have only 10 data points. Considering the relatively small scale of the simulation and the small number (10) of runs in this set our result is acceptable. Given more time and sets of a hundred runs on bigger sets of stars one can expect to improve this to match (61) better.

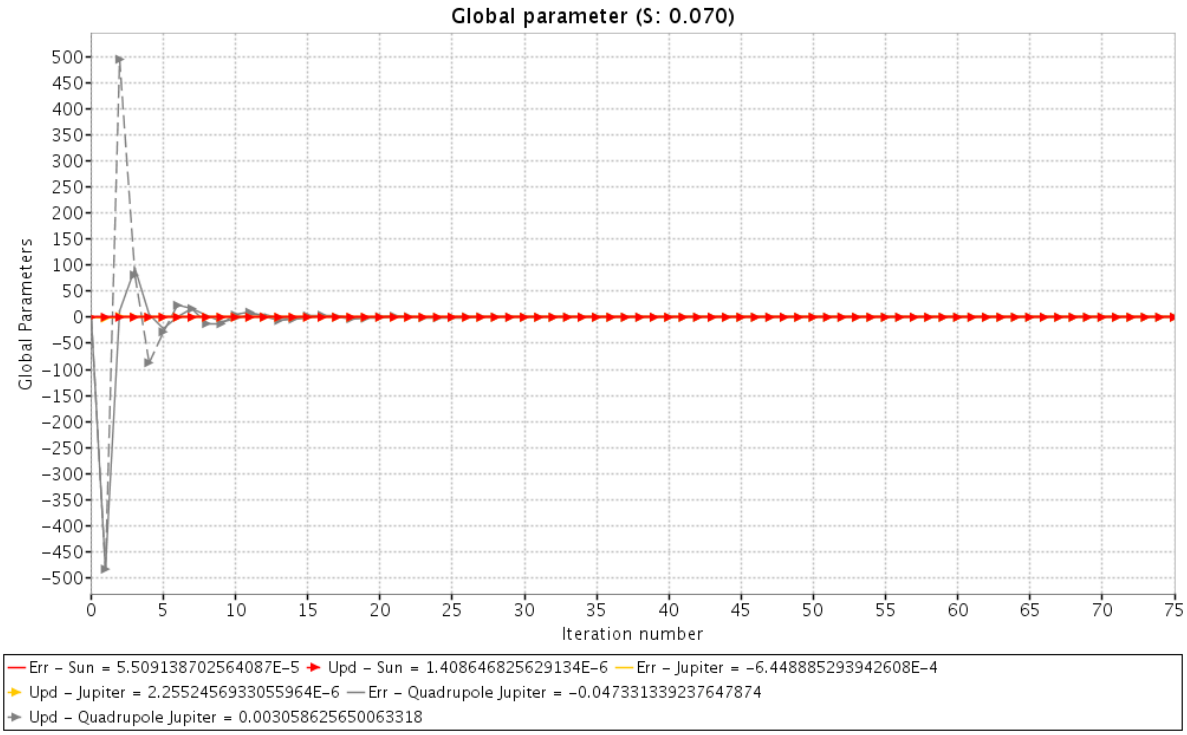

Figure 18: Convergence plot for the global parameters, in red (→) the error in PPN γ of the Sun in yellow (→) the error in PPN γ of Jupiter, and in grey (→) the error in QEF ε of Jupiter. For an exclusion zone radius $\theta_e = 20$ arcsec, observation noise enabled, no initial errors for source parameters, but initial errors in attitude and global parameters. The numbers in the box at the bottom of the graphs indicate the values at the end of iteration 50. (Plot generated using AGISLab)

The dependence of standard deviation (σ_ε) on the angular radius (θ_e) is shown in figure 20. An increase can be seen, this was to be expected since the quadrupole deflection depends strongly on the separation from Jupiter ($1/b^3$ see section 3.4.3 of Ludl [2011]).

From these results we can expect a 10σ detection of quadrupole light deflection with Gaia. In the realistic case of 5 arcsec the standard deviation is larger and the confidence level may be around 6σ. (The calculations are done, data on the averages for $\theta_e = 5$ arcsec will soon be added).

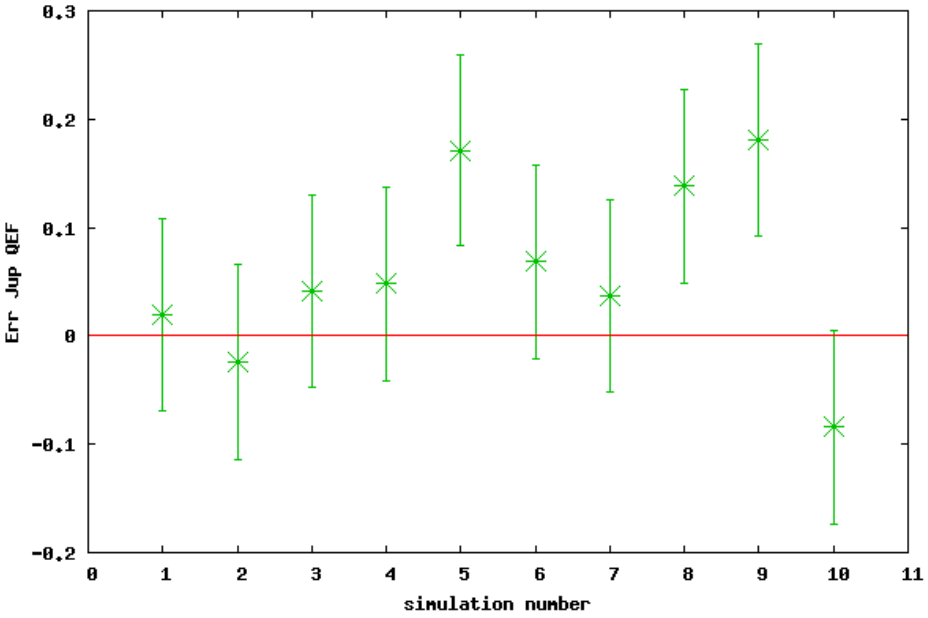

Figure 19: The distribution of errors (green crosses) $\mathrm{Err}_{\mathrm{Jup}}(\varepsilon)$, the error bars represent the formal standard deviations given by (60). For ten runs with observation noise enabled and zero exclusion radius. Different simulations use different seed values for the random sources and observation noise. The red line represents the expected value for the error in the baseline relativity model.

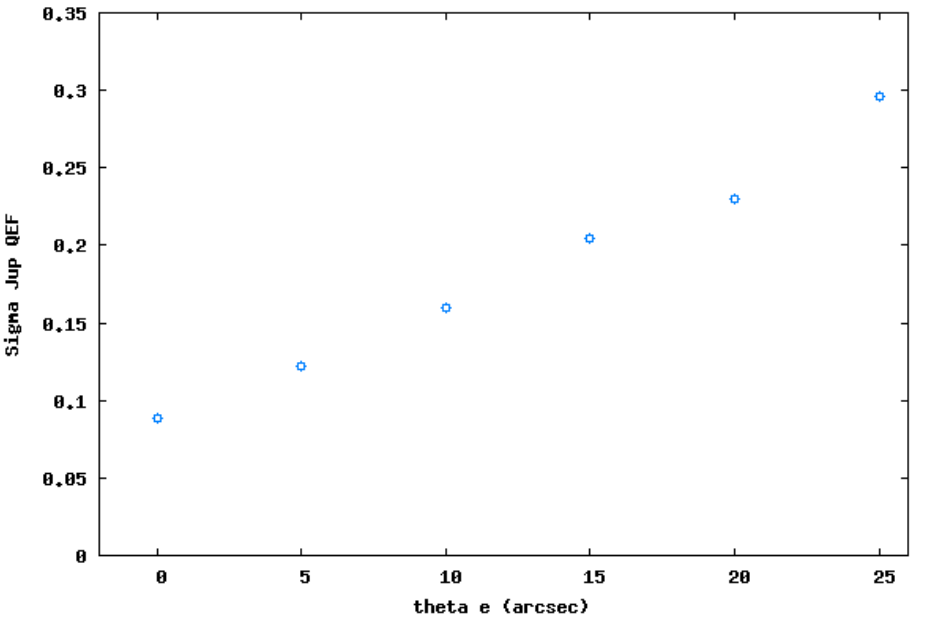

Figure 20: The standard deviation of QEF ε for Jupiter (σ_ε) as a function of the angular radius (θ_e) of the exclusion zone (in arcsec). For a given θ_e the values of σ_ε are very similar for different values of the random seeds. We have used averages over sets of ten simulations for $\theta_e = 0, 5, 15$ arcsec, and the values for a single simulation for the remaining cases.

4.2.3 Assessment of the monopole light deflection for the planets

In the first report we have discussed the convergence of the errors of PPN γ for small simulations. Here we analyse the results obtained for their standard errors in larger runs. We will give a realistic estimate of the precision of the measurement of PPN γ.

The size exclusion zone does not affect the precision of the convergence of PPN γ for the Sun and Jupiter as much as it does the quadrupole convergence. Since it is a stronger effect as discussed in section 3.4.4 of Ludl [2011].

The astrometric precision of these runs can be estimated from the results with $\theta_e = 0$ arcsec. An astrometric convergence plot is shown in figure 21. The configurations (set 3) have a flat convergence plot since we started from true source values (no inital errors). The astrometric precision is 10μarcsec. This is a good estimate of the end of mission accuracy of Gaia.

For the sets of 10 runs studied above ($\theta_e = 0$arcsec) with respect to QEF ε, we can also determine the errors in PPN γ using the same method. The results are shown in figures 22 and 23. For Jupiter we can note reasonable agreement, although the criterion (61) is only weakly fulfilled. $(\sigma_\gamma = 5.4 \cdot 10^{-4}; \sigma_\gamma^2 = 2.9 \cdot 10^{-7}; \left\langle \, \mathrm{Err}^2_{\mathrm{Jup}}(\gamma) \, \right\rangle = 4.6 \cdot 10^{-7})$

For the Sun we can see more outliers at the 1σ level. We note that the formal sigma $\sigma_{\gamma S} = 1.87 * 10^{-5}$ for PPN γ of the Sun is much smaller than those for γ and ε of Jupiter. We are already close to the limit of precision feasible with Gaia which is estimated to be $\sigma_\gamma > 10^{-6}$ (for PPN γ of the Sun) by Hobbs et al. [2010]. This again may be due to the small number of calcuations.

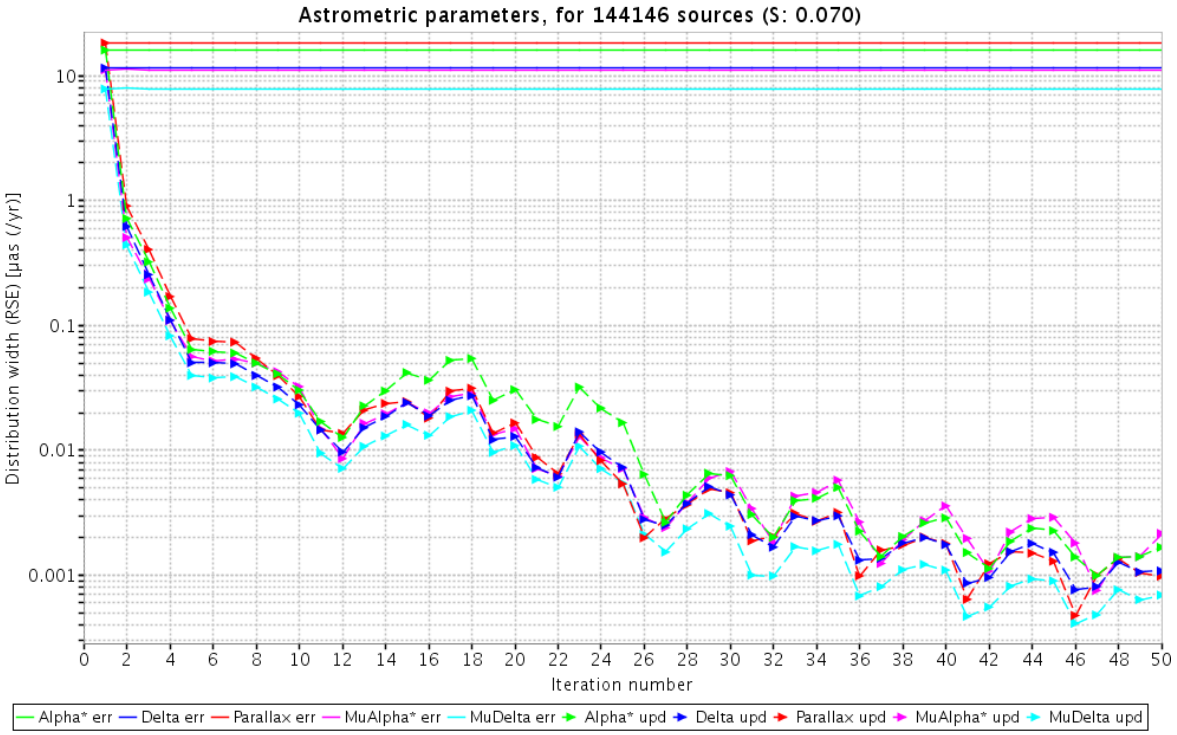

Figure 21: Convergence plot for the astrometric parameters, α (right ascension) in green, δ (declination) in blue, ϖ (parallax) in red, μ_α in pink and μ_δ in cyan. The solid line represents the value of the parameter and the dashed line shows the absolute value of the update of the parameter at each iteration. For an exclusion zone radius $\theta_e = 0$ arcsec, observation noise enabled, no initial errors for source parameters. The numbers in the box at the bottom of the graphs indicate the values at the end of iteration 50. (Plot generated using AGISLab)

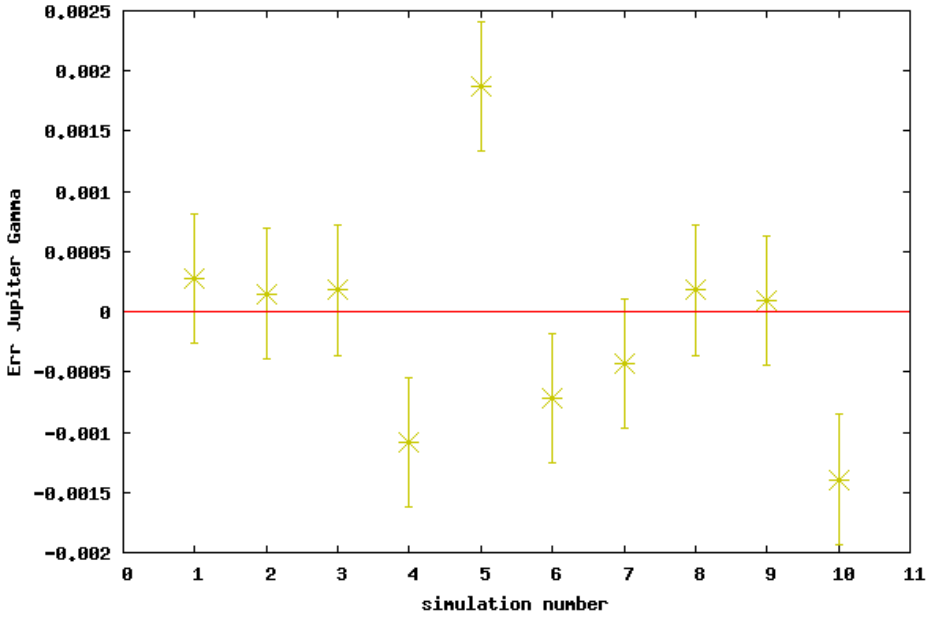

Figure 22: The distribution of errors (yellow crosses) $\mathrm{Err}_{\mathrm{Jup}}(\gamma)$, the error bars represent the formal standard deviations given by (60). For ten runs with observation noise enabled and zero exclusion radius. Different simulations use different seed values for the random sources and observation noise. The red line represents the expected value $\mathrm{Err}_{\mathrm{Jup}}(\gamma) = \gamma - 1 = 0$ for the error in the baseline relativity model.

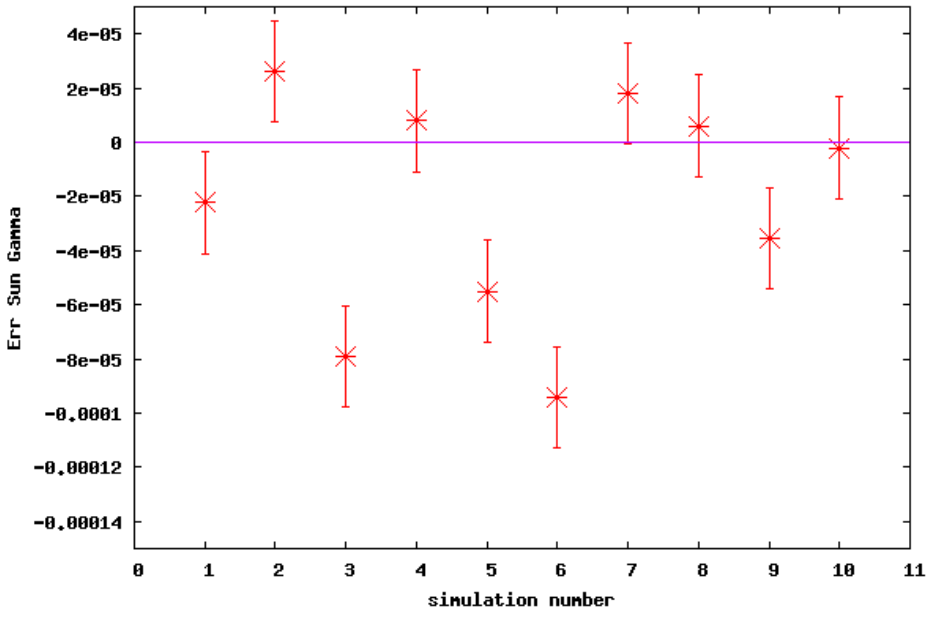

Figure 23: The distribution of errors (red crosses) $\mathrm{Err}_{\mathrm{Sun}}(\gamma)$ the error bars represent the formal standard deviations given by (60). For ten runs with observation noise enabled and zero exclusion radius. Different simulations use different seed values for the random sources and observation noise. The purple line represent the expected value $\mathrm{Err}_{\mathrm{Sun}}(\gamma) = \gamma - 1 = 0$ for the error in the baseline relativity model.

4.2.4 Discussion

According to these simulations, we can conclude that at a precision of 10μarcsec, Gaia will be able to measure deviations of PPN γ from the value it has in general relativity ($\gamma = 1$), if they are larger than 10^{-5}. However for the bound on Gaia, the number of stars and their weight matters strongly. Gaia is expected to see 100 million stars, our simulation is based on 140 thousand. The accuracy of the attitude will be much better for the real mission because Gaia will observe more bright stars all over the sky. There may not be many more stars close to Jupiter that will be observed, but the faint stars will also contribute to Gaia's final estimation of γ, albeit marginally, and can push the boundary of tests of alternative theories of gravity to 10^{-6} as demonstrated by [Hobbs et al., 2010].

We have also shown that a detection of quadrupole light deflection with Gaia is possible when accounting for realistic observation noise and an exclusion radius of $\theta_e = 5$ arcsecaround Jupiter. This is an improvement on the result of [Crosta and Mignard, 2006]They did not make realistic simulations of Gaia, no observation noise is included in their model, and they concluded only a 3σ confidence level of the detection. Concerning the determination of PPN γ with Jupiter's monopole deflection, we conclude that it will be possible to reach at least ($\sigma_\gamma = 5.4 \cdot 10^{-4}$) with real mission data. This is also an improvement on the 10^{-3} estimated by [Crosta and Mignard, 2006].

5 Conclusion

We have studied light deflection in the solar system from both the theoretical and practical perspectives. In the discussion of the theory we have focused on the model proposed by [Crosta and Mignard, 2006] and have deduced an expression for the derivative of the source direction with respect to the quadrupole efficiency factor (ε).

In the practical part of this work, we have focused on implementing this model accounting for quadrupole light deflection in AGISLab. Our results demonstrate that the scheme as implemented in AGISLab is reasonably well-behaved and converges. It allows to study light deflection in realistic simulations accounting for the exclusion zone near Jupiter and observation noise.

The framework that we have obtained will allow direct comparison of our results to those obtained with GREM and potentially other relativity models. They give a first estimation of Gaia's capacity to detect quadrupole light deflection by Jupiter. This we can answer in the affirmative, Gaia and AGIS will allow to detect this effect to at least 6σ level, when assuming nominal astrometric performance. We could also assess the impact of the size of the exclusion zone around Jupiter. From the results obtained we can conclude that detection quadrupole effect will suffer, but may be rendered unobservable should the radius of the exclusion zone exceed 20 arcsec.

Concerning the determination of PPN γ, our simulations indicate that Gaia should allow to detect variations down to at least $5.4 \cdot 10^{-4}$. On real Gaia data the result is presumably better, due to the larger number of sources observed all over the sky, solar (monopole) light deflection will be accurately constrained. As far as this Solar System test is concerned alternative theories of gravity will most likely have to stick closely to general relativity or be discarded.

As this is a short project, many paths had to be left unexplored and there are further topics to investigate. One interesting investigation would be to perform more runs to confirm the estimates of quadrupole detection presented in section 4.2.2. Also of interest is the impact of planetary light deflection affecting the monitoring of basic angle variations. This is possible because the parallax shift and light deflection from the Sun are nearly collinear. Thus terms allowing to de-correlate PPN γ from the parallax may help improve the uncertainties in the basic angle determination. Another topic closely related is dipole light deflection due to the motion of deflecting bodies and the integration of GREM into AGISLab.

Acknowledgements

I would like to thank my supervisor David Hobbs for proposing this exciting project and for his help along the way. His encouragement, his scientific advice, his effort and helpful implication have been invaluable. I am also grateful to my co-supervisor Lennart Lindegren for his accurate explanations and his comments which were always relevant, illuminating and demystifying. My thanks also go to Berry, Chris and Daniel for casual and helpful discussions about Gaia and AGIS.
In addition, I would like to express my gratitude to Ross Church and Johan Bijnens for valuable comments and discussions.

I would like to express my gratitude to Françoise Loytier and Sara Vilotti Pereira who have been of invaluable help during my stay in Lund. I would like to acknowledge also the help of Jean-Claude Mollier, my coordinator in Toulouse, who encouraged me to pursue physics.
My gratitude also goes to Melvyn B. Davies, the staff and students at Lund Observatory and Lund University for having made me feel welcome and the role they have played in my education.
I am grateful for the support of the *Agence pour l'enseigment français à l'étranger* over the five years of my studies in *classes préparatoires* and the *Ecole d'Ingénieur*.

To Alexey, Xinyi, Thomas, Charles, Sophia and Kristina go my sincere thanks for all the long conversations we have had about science, life and everything. They have been eye opening and I would not want to miss them. To all my friends go my thanks for cheering me up and for their understanding.
Most of all I would like to thank my family. My parents Elisabeth and Toni, and Ria and Werner for their support, their reliable advice, their kind words and for believing in me at all times.

References

Milton Abramowitz and Irene A. Stegun. *Handbook of Mathematical Functions with Formulas, Graphs, and Mathematical Tables*. Dover, New York, ninth dover printing, tenth gpo printing edition, 1964.

U. Bastian. Reference Systems, Conventions and Notations for Gaia. *Gaia Technical Note*, 07 2007.

A. Bombrun, L. Lindegren, B. Holl, and S. Jordan. Complexity of the Gaia astrometric least-squares problem and the (non-)feasibility of a direct solution method. A&A, 516:A77+, June 2010. doi: 10.1051/0004-6361/200913503.

M. Crosta. Tracing light propagation to the intrinsic accuracy of space-time geometry. *ArXiv e-prints*, December 2010.

M. Crosta and A. Vecchiato. Gaia relativistic astrometric models. I. Proper stellar direction and aberration. A&A, 509:A37+, January 2010. doi: 10.1051/0004-6361/200912691.

M. T. Crosta and F. Mignard. Microarcsecond light bending by Jupiter. *Classical and Quantum Gravity*, 23:4853–4871, August 2006. doi: 10.1088/0264-9381/23/15/006.

Jos de Bruijne. Along- and across-scan location-estimation performance, 07 2009. URL `http://www.rssd.esa.int/llink/livelink/open/2913726`.

ESA Science Team. Gaia information sheets. ESA Gaia mission website, 2010. `http://www.rssd.esa.int/index.php?project=GAIA&page=Info_sheets_overview`.

A. Fienga, H. Manche, J. Laskar, and M. Gastineau. INPOP06: a new numerical planetary ephemeris. A&A, 477:315–327, January 2008. doi: 10.1051/0004-6361:20066607.

E. B. Fomalont and R. A. Sramek. Measurements of the solar gravitational deflection of radio waves in agreement with general relativity. *Physical Review Letters*, 36:1475–1478, June 1976. doi: 10.1103/PhysRevLett.36.1475.

B. Guinot. Résolution A4(1991), Union Astronomique Internationale, sur les systèmes de référencé: echelles de temps. In *Journées 1992: Systèmes de référence spatio-temporels*, pages 12–21, 1992.

D. Hobbs, B. Holl, L. Lindegren, F. Raison, S. Klioner, and A. Butkevich. Determining PPN γ with Gaia's astrometric core solution. In S. A. Klioner, P. K. Seidelmann, & M. H. Soffel, editor, *IAU Symposium*, volume 261 of *IAU Symposium*, pages 315–319, January 2010. doi: 10.1017/S1743921309990561.

B. Holl, D. Hobbs, and L. Lindegren. Spatial correlations in the Gaia astrometric solution. In S. A. Klioner, P. K. Seidelmann, & M. H. Soffel, editor, *IAU Symposium*, volume 261 of *IAU Symposium*, pages 320–324, January 2010. doi: 10.1017/S1743921309990573.

C. Jordi, M. Gebran, J. M. Carrasco, J. de Bruijne, H. Voss, C. Fabricius, J. Knude, A. Vallenari, R. Kohley, and A. Mora. Gaia broad band photometry. A&A, 523:A48+, November 2010. doi: 10.1051/0004-6361/201015441.

S. A. Klioner. A Practical Relativistic Model for Microarcsecond Astrometry in Space. AJ, 125:1580–1597, March 2003.

S. A. Klioner. Gaia relativity model: concise description. *Gaia Technical Note*, 2008.

S. M. Kopeikin and V. V. Makarov. Gravitational bending of light by planetary multipoles and its measurement with microarcsecond astronomical interferometers. Phys. Rev. D, 75 (6):062002–+, March 2007. doi: 10.1103/PhysRevD.75.062002.

J. Kovalevsky. *Modern Astrometry*. 2002.

U. Lammers and L. Lindegren. News on Seeking Gaia's Astrometric Core Solution with AGIS. In *EAS Publications Series*, volume 45, pages 123–126, February 2011. doi: 10.1051/eas/1045021.

L. D. Landau and E. M. Lifshitz. *The classical theory of fields*. 1975.

M.G. Lattanzi and M.-T. Crosta. Implementation of the quadrupole deflection experiment in DPAC (GA REQ), November 2009. URL `http://www.rssd.esa.int/llink/livelink/open/2941668`.

Adrien-Marie Le Gendre. Recherches sur l'attraction des sphéroïdes homogènes (*Studies on the attraction of homogeneous spheroids*). *Mémoires de Mathématiques et de Physique, présentés à l'Académie royale des sciences (Paris) par sçavants étrangers*, 10:411–435, 1782.

L. Lindegren. Proposed prototype processes for the GAIA Global Iterative Solution, March 2001. URL `http://www.rssd.esa.int/llink/livelink/open/357825`.

L. Lindegren and U. Bastian. Basic principles of scanning space astrometry. In *EAS Publications Series*, volume 45, pages 109–114, February 2011. doi: 10.1051/eas/1045018.

L. Lindegren, E. Hog, F. van Leeuwen, C. A. Murray, D. W. Evans, M. J. Penston, M. A. C. Perryman, C. Petersen, N. Ramamani, and M. A. J. Snijders. The NDAC HIPPARCOS data analysis consortium - Overview of the reduction methods. A&A, 258:18–30, May 1992.

L. Lindegren, U. Lammers, D. Hobbs, W. O'Mullane, U. Bastian, and J. Hernandez. The astrometric core solution for the Gaia mission, Overview of models, algorithms and software implementation. submitted August 2011.

A.-A. Ludl. Investigating Mono– and Quadrupole Gravitational Light Deflection by Jupiter. Degree project thesis, 2011-EXA57, Lund University, 2011.

J.M. Martin Fleitas, A. Mora, F. Raison, et al. VPU. Object detectability near bright extended sources. The Jupiter case, February 2011. URL `http://www.rssd.esa.int/llink/livelink/open/3061697`.

F. Mignard. Fundamental Physics with GAIA. In O. Bienayme & C. Turon, editor, *EAS Publications Series*, volume 2, pages 107–121, 2002.

M. Perryman. *The Making of History's Greatest Star Map*. 2010.

T. Prusti. General status of the Gaia mission and expected performance. In *EAS Publications Series*, volume 45, pages 9–14, February 2011. doi: 10.1051/eas/1045002.

I.W. Roxburgh. Gravitational multipole moments of the Sun determined from helioseismic estimates of the internal structure and rotation. *Astron. Astrophys.*, 377:688–690, 2001. doi: 10.1051/0004-6361:20011104.

P. Schneider, J. Ehlers, and E. E. Falco. *Gravitational Lenses*. 1992.

R. U. Sexl and H. Sexl. *White dwarfs-black holes: an introduction to relativistic astrophysics*. 1979.

J. M. Weisberg and J. H. Taylor. The Relativistic Binary Pulsar B1913+16: Thirty Years of Observations and Analysis. In F. A. Rasio & I. H. Stairs, editor, *Binary Radio Pulsars*, volume 328 of *Astronomical Society of the Pacific Conference Series*, pages 25–+, July 2005.

Clifford M. Will. The Confrontation between General Relativity and Experiment. *Living Reviews in Relativity*, 9(3), 2006. URL `http://www.livingreviews.org/lrr-2006-3`.

Clifford M. Will. On the unreasonable effectiveness of the post-Newtonian approximation in gravitational physics. *Proceedings of the National Academy of Sciences*, 2011. doi: 10.1073/pnas.1103127108. URL `http://www.pnas.org/content/early/2011/03/28/1103127108.abstract`.

C.M. Will. *Theory and Experiment in Gravitational Physics*. Cambridge University Press, Cambridge; New York, 2nd edition, 1993.

S. Zschocke and S. A. Klioner. On the efficient computation of the quadrupole light deflection. *Classical and Quantum Gravity*, 28(1):015009–+, January 2011. doi: 10.1088/0264-9381/28/1/015009.

A Acronyms and Notations

Abbreviation	Meaning
AC	across-scan
AGIS	Astrometric Global Iterative Solution
AL	along-scan
as or $''$	second of arc or arcsecond (arcsec), 1 part in 3600 of one degree
AU	astronomical unit
BCRS	Barycentric Reference System
ESAC	European Space Astronomy Centre (ESAC), near Madrid
CoMRS	Center-of-Mass Reference System (of Gaia)
FL	First-Look
FoV	field of view
Gaia	(formerly) Global Astrometric Interferometer for Astrophysics
GCRS	Geocentric Reference System
Hipparcos	High Precision Parallax Collecting Satellite
IAU	International Astronomical Union
ICRS	International Celestial Reference System
ICRF	International Celestial Reference Frame
IDT	Initial Data Treatment
IMCCE	Institut de Mécanique Céleste et de Calcul des Éphémérides, Paris
ISO	International Organisation for Standardization, Geneva
JD	Julian Date; a notation for time
JPL	Jet Propulsion Laboratory, NASA, Pasadena
ODAS	One Day Astrometric Solution
PPN	parametrized post-Newtonian
μarcsec	micro arcsecond
QEF	quadrupole efficiency factor

Table 5: The listing of the acronyms used in this work.

B Tensor equations

B.1 Covariant derivative and Christoffel symbols

For partial derivatives we use the following notation :

$$\partial_\beta A_\alpha \quad := \quad \frac{\partial}{\partial x^\beta} A_\alpha \tag{62}$$

Some authors also use the notation $A_{\alpha\,,\beta} = \partial_\beta A_\alpha$ which we have avoided here. In tensorial equations, we use the Einstein summation convention. Greek indeces range from 0 to 3, latin indices from 1 to 3. The Christoffel symbols $\Gamma^\alpha_{\beta\gamma}$ (also called connection coefficients):

are defined by (63). Relation (64) relates it to the metric tensor.

$$\Gamma^\alpha_{\beta\gamma} \quad = \quad -\,\partial_\beta \bar{x}^\mu \partial_\gamma \bar{x}^\nu \partial_{\bar{\mu}} \partial_{\bar{\nu}} x^\alpha \tag{63}$$

$$\Gamma^\alpha_{\beta\gamma} \quad = \quad \frac{1}{2}\, g_{\nu\mu}\,(\,\partial_\beta g_{\mu\alpha} + \partial_\alpha g_{\mu\beta} - \partial_\mu g_{\alpha\beta}\,) \tag{64}$$

We define the covariant derivative of a covariant tensor A_α by

$$A_{\alpha;\,\beta} \quad = \quad \partial_\beta A_\alpha + \Gamma^\nu_{\alpha\beta} A_\nu \tag{65}$$

B.2 Riemann and Einstein tensors

The Riemann curvature tensor $R^{\mu}_{\nu\alpha\beta}$, which is a function of the Christoffel symbols and therefore of the metric itself.

$$R^{\mu}_{\nu\alpha\beta} = \partial_{\alpha}\Gamma^{\mu}_{\nu\beta} - \partial_{\beta}\Gamma^{\mu}_{\nu\alpha} + \Gamma^{\mu}_{\gamma\alpha}\Gamma^{\gamma}_{\nu\beta} - \Gamma^{\mu}_{\gamma\beta}\Gamma^{\gamma}_{\nu\alpha} \tag{66}$$

as given in [Will, 1993] section 3.2
The Einstein tensor $G_{\mu\nu}$ is defined as:

$$G_{\mu\nu} = R_{\mu\nu} - \frac{1}{2}g_{\mu\nu}R \tag{67}$$

where $R_{\alpha\beta}$ and R are defined as contractions of the Riemann curvature tensor. The Ricci tensor is $R_{\alpha\beta} = R^{\nu}_{\alpha\nu\beta}$ and the Ricci scalar is $R = g^{\alpha\beta}R_{\alpha\beta}$.

B.3 Energy-momentum tensor

The energy momentum tensor appearing the in the field equations (2) will depend on the model of matter chosen. A fairly general example is given by [Will, 1993], where matter is modeled as a perfect fluid in which case:

$$T^{\mu\nu} = (\,\rho + \rho\Pi + p\,)\,u^{\mu}u^{\nu} + p\,g^{\mu\nu} \tag{68}$$

where the quantities are defined as follows:

- ρ is rest-mass–energy density of atoms in the fluid element,
- p is the isotropic pressure of the fluid,
- Π is the specific density of internal kinetic and thermal energy,
- $u^{\mu} = dx^{\mu}/d\tau$ is the four-velocity vector of the fluid element.

and τ is the separation between two space-time events:

$$d\tau^2 = \epsilon\, g^{\mu\nu}x^{\mu}x^{\nu} \tag{69}$$

$$\tau = \int_{Path:a\to b} d\tau \tag{70}$$

where $\epsilon = \pm 1$ is chosen so that $d\tau^2$ is positive. The separation between two events is called time-like if $\epsilon = -1$ and space-like otherwise. If $g^{\mu\nu}x^{\mu}x^{\nu} = 0$ the separation is called light-like, since light rays move along these null trajectories.

C Units

In this work we use SI units [10] . It is noteworthy that units are locally defined as "proper units" in a reference frame. The question of their use and interpretation in general relativistic context is discussed in the IAU resolution of 1991 Guinot [1992].

quantity	unit	value
G	$[m^3kg^{-1}s^{-2}]$	$6.67428 \cdot 10^{-11}$
c	$[ms^{-1}]$	$2.99792458 \cdot 10^{8}$
a	$[m\,AU^{-1}]$	$1.49597870691 \cdot 10^{11}$

Table 6: Values of constants used in AGIS and AGISLab, provided by the Gaia Parameter Database (`http://gaia.esac.esa.int/gpdb`).

[10] *Système International* `http://www.bipm.org/en/si/`

D Legendre polynomials

The Legendre polynomials are given by the concise explicit expression (71):

$$P_n(y) = \frac{1}{2^n(n!)}\partial_y^n\left[\left(y^2-1\right)^n\right] \tag{71}$$

$$(n+1)P_{n+1}(y) = (2n+1)yP_n(y) - nP_{n-1}(y) \tag{72}$$

where n is a positive integer number. Relation (72) is called Bonnet's recursion formula.

These mathematical results can be found at `http://dlmf.nist.gov/` and Abramowitz and Stegun [1964] chapter 8.

The following are the first four polynomials which are used in the calculation in section 3.2.3.

$$P_0(y) = 1 \tag{73}$$
$$P_1(y) = y \tag{74}$$
$$P_2(y) = \frac{1}{2}\left(3y^2-1\right) \tag{75}$$
$$P_3(y) = \frac{1}{2}\left(5y^3-3y\right) \tag{76}$$

E Addenda

E.1 Plots of the errors for 5 arcsec exclusion radius

The figures below illustrate the errors and standard deviations of the quadrupole efficiency factor ε, and PPN γ for the Sun and Jupiter. They correspond to a value of the exclusion radius around Jupiter $\theta_e = 5$ arcsec. These 10 simulations use the configuration of case 4 in table 4 , 5 arcsec. Figures 33, 34 and 35 are the respective counterparts of figures 27, 29 and 30 given in section 4.2.2 and 4.2.3.

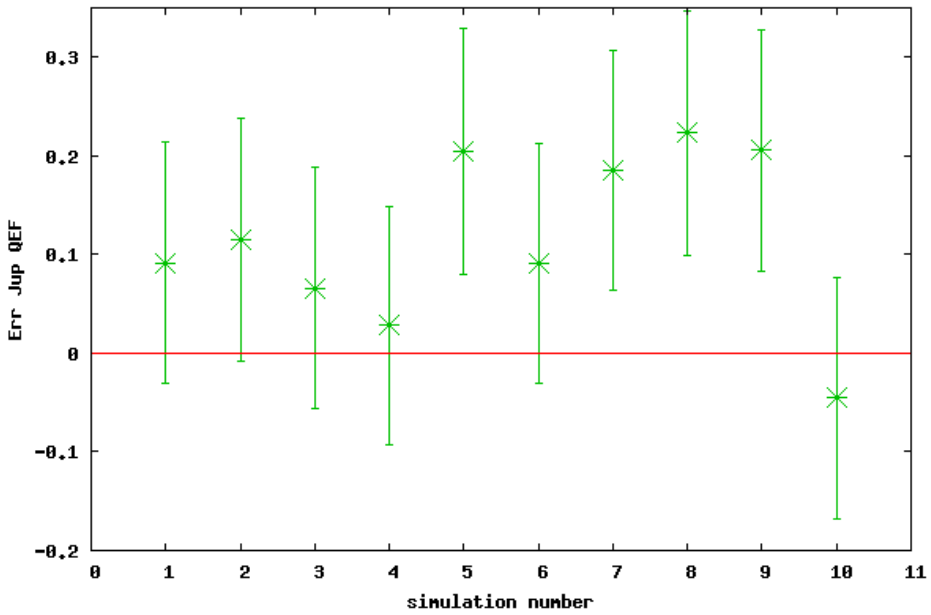

Figure 24: The distribution of errors (green crosses) $\mathrm{Err}_{\mathrm{Jup}}(\varepsilon)$, the error bars represent the formal standard deviations given by (60). For ten runs with observation noise enabled and 5 arcsec exclusion radius. Different simulations use different seed values for the random sources and observation noise. The red line represents the expected value for the error in the baseline relativity model.

We see that there are more outliers in this case. It could be that the errors are not fully converged, the exclusion zone angle might influence the convergence of the global parameters. Alternatively, the sample of 10 runs may be too small.

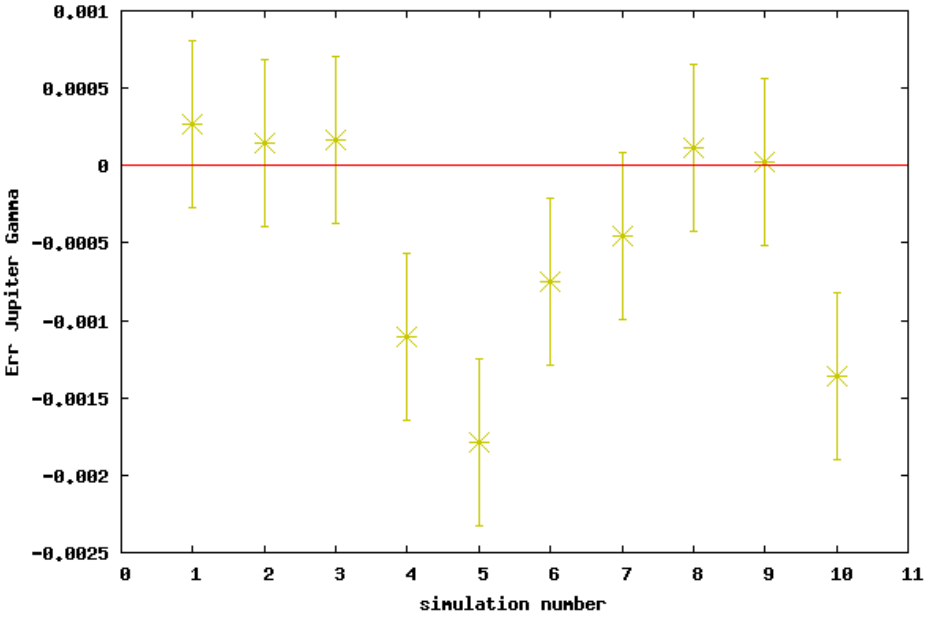

Figure 25: The distribution of errors (yellow crosses) $\mathrm{Err}_{\mathrm{Jup}}(\gamma)$, the error bars represent the formal standard deviations given by (60). For ten runs with observation noise enabled and 5 arcsec exclusion radius. Different simulations use different seed values for the random sources and observation noise. The red line represents the expected value for the error in the baseline relativity model.

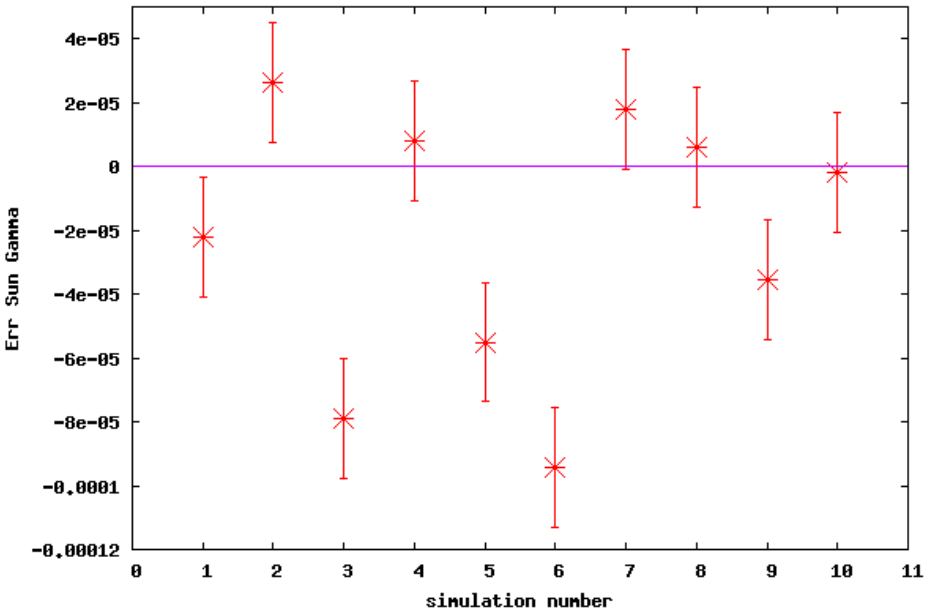

Figure 26: The distribution of errors (green crosses) $\mathrm{Err}_{\mathrm{Sun}}(\gamma)$, the error bars represent the formal standard deviations given by (60). For ten runs with observation noise enabled and 5 arcsec exclusion radius. Different simulations use different seed values for the random sources and observation noise. The red line represents the expected value for the error in the baseline relativity model.

E.2 Sky plot of a simulation with set 3

In figure 27 the sky map of astrometric errors in parallax ϖ is shown. These charts were produced with simulations of case 4 (set 3 and 70 thousand random stars). They do show that the presence of the random stars does deteriorate the precision of the astrometric solution much. The maximal errors are about 20 μarcsecbut they are rare, this is in good agreement with nominal Gaia performance.

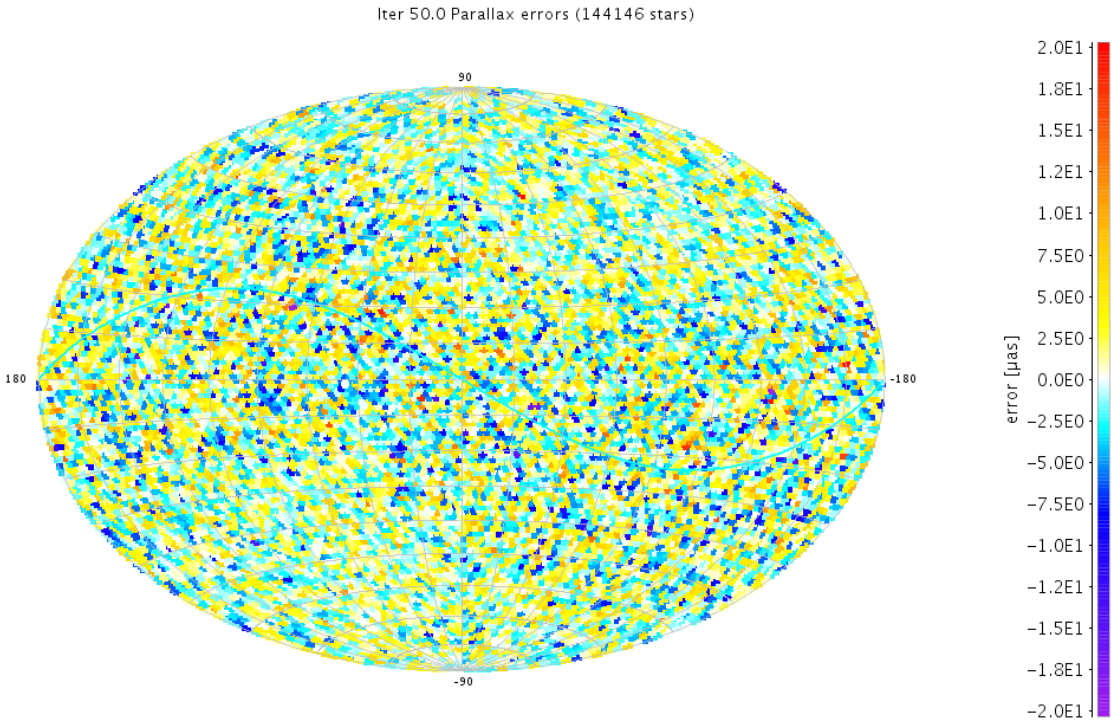

Figure 27: Sky map showing the average error per pixel of the parallax ϖ at iteration 50. (For the projection the equatorial coordinate system is used.) [image generated with AGISLab]

E.3 The quadrupole deflection pattern near Jupiter.

The figure below shows the quadrupole light deflection pattern near Jupiter. The corresponding figure of the monopole deflection is shown in figure 15 section 3.4.3 in Ludl [2011].

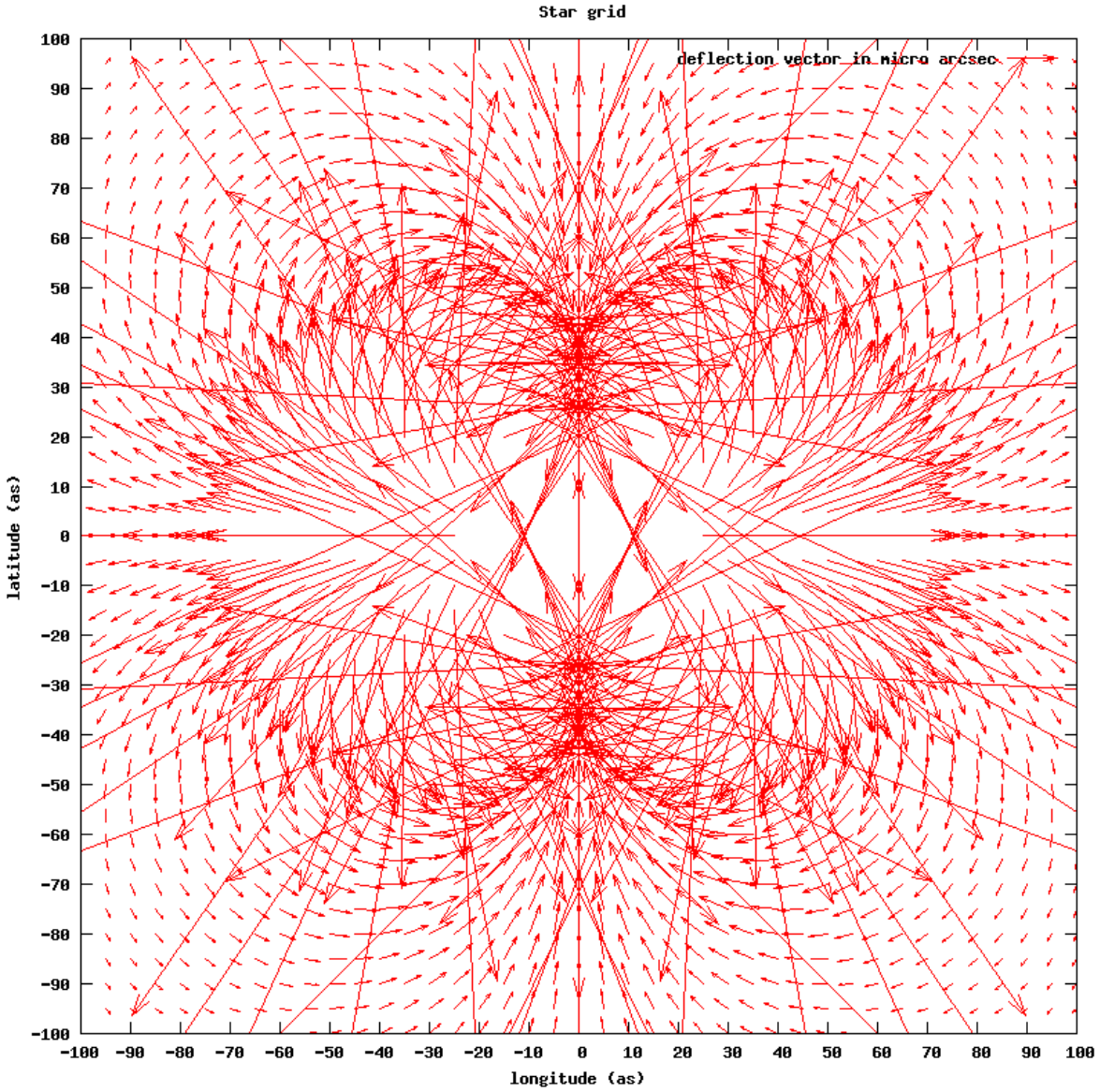

Figure 28: The quadrupole deflection for a star grid centered on Jupiter (40 × 40 stars, separation 5 arcsec). This shows a zoom on the inner 200 arcsec. (The scale of the arrows is in micro arcsec, i.e. they have been scaled up by a factor of 10^6 compared to the angular scale.) The data was computed using the tests for quadrupole deflection presented in section 3.4 of Ludl [2011]. [image generated with Gnuplot]